

Optical trapping by Laguerre-Gaussian beams: Symmetries, stability and equilibria

Alexei D. Kiselev^{1,*} and Dmytro O. Plutenko^{2,3,†}

¹*Saint Petersburg National Research University of Information Technologies,
Mechanics and Optics (ITMO University),*

Kronverskyi Prospekt 49, 197101 St Petersburg, Russia

²*Institute of Physics of National Academy of Sciences of Ukraine,
prospekt Nauki 46, 03680 Kiev, Ukraine*

³*Physical Engineering Teaching Research Center of
National Academy of Sciences of Ukraine, Kiev, Ukraine*

(Dated: February 12, 2022)

By using the method of far-field matching we obtain the far-field expressions for the optical (radiation) force exerted by Laguerre–Gaussian (LG) light beams on a spherical (Mie) particle and study the optical-force-induced dynamics of the scatterer near the trapping points represented by the equilibrium (zero-force) positions. The regimes of linearized dynamics are described in terms of the stiffness matrix spectrum and the damping constant of the ambient medium. Numerical analysis is performed for both non-vortex and optical vortex LG beams. For the purely azimuthal LG beams, the dynamics is found to be locally non-conservative and is characterized by the presence of conditionally stable equilibria (unstable zero-force points that can be stabilized by the ambient damping). We also discuss effects related to the Mie resonances (maxima of the internal field Mie coefficients) that under certain conditions manifest themselves as the points changing the trapping properties of the particles.

PACS numbers: 42.50.Wk, 42.25.Fx, 42.68.Mj, 87.80.Cc

Keywords: optical (radiation) force; light scattering; Laguerre–Gaussian beams; optical vortices; stiffness matrix

I. INTRODUCTION

The idea of a mechanical action of light has been pursued for hundreds of years. In the 1970s Ashkin demonstrated the fact that focused laser beams can be used to trap and control dielectric particles, which also included feedback cooling [1, 2]. Over the past two decades single-beam optical traps, that were first developed in [3] and are commonly known as the optical tweezers, have become an indispensable tool in numerous fields of science where optical forces are employed for manipulation, measurements, or for creating and controlling new states of matter.

Theoretical approaches to modeling of optical tweezers are typically based on the theory of light scattering [4, 5] and use the methods closely related to the problem of light scattering by spherically shaped particles that dates back to the more than century-old classical exact

* Email address: alexei.d.kiselev@gmail.com

† Email address: dmplutenko@gmail.com

solution due to Mie [6]. A systematic expansion of the electromagnetic field over vector spherical harmonics lies at the heart of Mie-type theories [7–10].

The specific form of the expansions known as the T -matrix ansatz has been widely used in the related problem of light scattering by non-spherical [9, 11, 12] and optically anisotropic particles [13–17]. Light scattering from arbitrary shaped laser beams [18–22] has been the key subject of the Mie-type theory — the so-called generalized Lorenz–Mie theory (GLMT) — extended to the case of arbitrary incident-beam scattering [10, 23].

In GLMT, illuminating beams are described in terms of expansions over a set of basis wavefunctions and the expansion coefficients known as the *beam shape coefficients* [24]. When the analytical treatment of laser beams uses approximations such as the well-known paraxial approximation [25], the key difficulty is that multipole expansions for approximate solutions of the vector Helmholtz equation (pseudo-fields) representing the beams do not exist. Therefore, some remodelling procedure must be invoked to obtain a real radiation field.

Typically, remodelling procedure assume that the actual incident field is equal to the pseudo-field on a matching surface such as a far-field sphere [26], the focal plane [26, 27], and a Gaussian reference sphere representing a lens [28]. Given the pseudo-field distribution on the surface, the beam shape coefficients then can be evaluated using either numerical integration or the one-point matching method [26].

Alternatively, propagation of a laser beam, which is known in the paraxial limit, can be analytically described without recourse to the paraxial approximation. In Refs. [29–33] this strategy has been applied to the important case of Laguerre–Gaussian (LG) beams using different methods.

In recent studies of light scattering by spherical and spheroidal particles illuminated with LG beams [34, 35], the analytical results of Ref. [31] were used to calculate the beam shape coefficients. In our previous paper [36] the far-field matching method is combined with the results for nonparaxial propagation of LG beams [32, 33] to study near-field structures such as nanojets and optical vortices. Similar method was recently used in Ref. [37].

LG beams are important for optical trapping [38]. At nonzero azimuthal mode number, they represent optical vortex laser beams exhibiting a helical phase front and carrying a phase singularity. The topological charge of the phase singularity and associated orbital angular momentum are known to give rise to a number of distinctive phenomena [39, 40]. In particular, rotation of trapped spheres by vortex beams [41, 42] is a remarkable manifestation of the non-conservative nature of optical-force-induced dynamics. The latter implies that, owing to a scattering contribution to optical force fields, the optical forces cannot generally be derived from an underlying potential. This has important consequences for stochastic dynamics of the particles optically trapped by LG beams. In particular, such particles may not approach thermodynamic equilibrium [43–46]. The fundamental problems of nonequilibrium statistical physics [47, 48] have thus given additional impetus to the studies on technologically important subject related to dynamics of optical trapping.

In this paper we deal with the radiation-force-induced dynamics of Mie scatterers. Our goal is to examine the regimes of the dynamics depending on the parameters characterizing both the LG beam and the scatterer. For this purpose, we systematically use the far-field matching method supplemented with the symmetry analysis. The effects related to the non-conservative character of the dynamics and the role of Mie resonances will be of our primary interest.

The layout of the paper is as follows. In Sec. II, we outline our theoretical approach. The

analytical results for the beam shape coefficients of LG beams and the fundamental properties of the far-field angular distributions are described in Sec. III. The far-field expressions for the flux of the Poynting vector and the optical force are deduced in Sec. IV A. Symmetry analysis for LG beams is performed in Sec. IV B. The optical-force-induced dynamics and stability of the zero-force points are discussed in Sec. V A. In the remaining part of Sec. V, we present the results of numerical computations such as the stiffness matrix eigenvalues and the on-axis position of the equilibria evaluated as a function of the scatterer size parameter at different values of the LG beam radial and azimuthal mode numbers. Technical details on separating out the gradient dependent terms in the expression for the optical force are relegated to Appendix A. Finally, in Sec. VI, we draw our results together and make some concluding remarks.

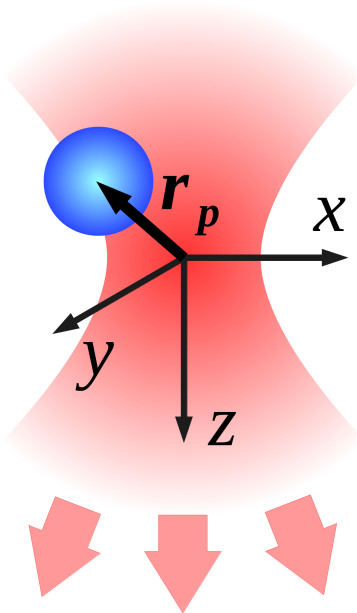


Figure 1: (Color online) Mie scatterer (spherical particle) is illuminated with a focused LG beam propagating along the z axis. The displacement vector \mathbf{r}_p determines location of the particle with respect to the beam waist.

II. LORENZ–MIE THEORY: WAVE FUNCTIONS AND T –MATRIX

In this section we introduce all necessary notations and briefly discuss how the properties of Mie scattering can be described in terms of the T –matrix [7, 9]. Our formulation closely follows to the line of our presentation given in Refs. [14, 36].

We consider scattering by a spherical particle of radius R_p embedded in a uniform isotropic dielectric medium with dielectric constant ϵ_{med} and magnetic permeability μ_{med} (the geometry of light scattering is schematically illustrated in Fig. 1). The dielectric constant and magnetic permittivity of the particle are ϵ_p and μ_p , respectively. For a harmonic electromagnetic wave (time–dependent factor is $\exp\{-i\omega t\}$), the Maxwell equations can be written in

the following form:

$$-ik_i^{-1} \nabla \times \mathbf{E} = \frac{\mu_i}{n_i} \mathbf{H}, \quad (1a)$$

$$ik_i^{-1} \nabla \times \mathbf{H} = \frac{n_i}{\mu_i} \mathbf{E}, \quad i = \begin{cases} \text{med}, & r > R_p \\ p, & r < R_p \end{cases} \quad (1b)$$

where $n_{\text{med}} = \sqrt{\epsilon_{\text{med}} \mu_{\text{med}}}$ is the refractive index outside the scatterer (in the ambient medium), where $r > R_p$ ($i = \text{med}$) and $k_i = k_{\text{med}} = n_{\text{med}} k_{\text{vac}}$ ($k_{\text{vac}} = \omega/c = 2\pi/\lambda$ is the free-space wave number); $n_p = \sqrt{\epsilon_p \mu_p}$ is the refractive index for the region inside the spherical particle (scatterer), where $r < R_p$ ($i = p$) and $k_i = k_p = n_p k_{\text{vac}}$.

The electromagnetic field can always be expanded using the vector spherical harmonic basis [49]. There are three cases of these expansions that are of particular interest. They correspond to the incident wave, $\{\mathbf{E}_{\text{inc}}, \mathbf{H}_{\text{inc}}\}$, the outgoing scattered wave, $\{\mathbf{E}_{\text{sca}}, \mathbf{H}_{\text{sca}}\}$ and the electromagnetic field inside the scatterer, $\{\mathbf{E}_p, \mathbf{H}_p\}$:

$$\mathbf{E}_\alpha = \sum_{jm} [\alpha_{jm}^{(\alpha)} \mathbf{M}_{jm}^{(\alpha)}(\rho_i, \hat{\mathbf{r}}) + \beta_{jm}^{(\alpha)} \mathbf{N}_{jm}^{(\alpha)}(\rho_i, \hat{\mathbf{r}})], \quad \alpha \in \{\text{inc}, \text{sca}, p\} \quad (2a)$$

$$\mathbf{H}_\alpha = n_i/\mu_i \sum_{jm} [\alpha_{jm}^{(\alpha)} \mathbf{N}_{jm}^{(\alpha)}(\rho_i, \hat{\mathbf{r}}) - \beta_{jm}^{(\alpha)} \mathbf{M}_{jm}^{(\alpha)}(\rho_i, \hat{\mathbf{r}})], \quad (2b)$$

$$\mathbf{M}_{jm}^{(\alpha)}(\rho_i, \hat{\mathbf{r}}) = ik_i^{-1} \nabla \times \mathbf{N}_{jm}^{(\alpha)} = z_j^{(\alpha)}(\rho_i) \mathbf{Y}_{jm}^{(m)}(\hat{\mathbf{r}}), \quad (2c)$$

$$\mathbf{N}_{jm}^{(\alpha)}(\rho_i, \hat{\mathbf{r}}) = -ik_i^{-1} \nabla \times \mathbf{M}_{jm}^{(\alpha)} = \frac{\sqrt{j(j+1)}}{\rho_i} z_j^{(\alpha)}(\rho_i) \mathbf{Y}_{jm}^{(0)}(\hat{\mathbf{r}}) + Dz_j^{(\alpha)}(\rho_i) \mathbf{Y}_{jm}^{(e)}(\hat{\mathbf{r}}), \quad (2d)$$

$$i = \begin{cases} \text{med}, & \alpha \in \{\text{inc}, \text{sca}\} \\ p, & \alpha = p \end{cases}, \quad z_j^{(\alpha)}(\rho_i) = \begin{cases} j_j(\rho), & \alpha = \text{inc} \\ h_j^{(1)}(\rho), & \alpha = \text{sca} \\ j_j(\rho_p), & \alpha = p \end{cases} \quad (2e)$$

where $\rho \equiv \rho_{\text{med}} = k_{\text{med}} r$, $\rho_p = k_p r \equiv n\rho$, and $n = n_p/n_{\text{med}}$ is the ratio of refractive indexes also known as the *optical contrast*; $Df(x) \equiv x^{-1} \partial_x(xf(x))$ and ∂_x stands for a derivative with respect to x .

According to Ref. [14], the spherical harmonics can be conveniently expressed in terms of the Wigner D -functions [49, 50] as follows

$$\mathbf{Y}_{jm}^{(m)}(\hat{\mathbf{r}}) = N_j/\sqrt{2} \{D_{m,-1}^{j*}(\hat{\mathbf{r}}) \mathbf{e}_{-1}(\hat{\mathbf{r}}) - D_{m,1}^{j*}(\hat{\mathbf{r}}) \mathbf{e}_{+1}(\hat{\mathbf{r}})\}, \quad (3a)$$

$$\mathbf{Y}_{jm}^{(e)}(\hat{\mathbf{r}}) = N_j/\sqrt{2} \{D_{m,-1}^{j*}(\hat{\mathbf{r}}) \mathbf{e}_{-1}(\hat{\mathbf{r}}) + D_{m,1}^{j*}(\hat{\mathbf{r}}) \mathbf{e}_{+1}(\hat{\mathbf{r}})\}, \quad (3b)$$

$$\mathbf{Y}_{jm}^{(0)}(\hat{\mathbf{r}}) = N_j D_{m,0}^{j*}(\hat{\mathbf{r}}) \mathbf{e}_0(\hat{\mathbf{r}}) = Y_{jm}(\hat{\mathbf{r}}) \hat{\mathbf{r}}, \quad N_j = [(2j+1)/4\pi]^{1/2}, \quad (3c)$$

where $\mathbf{Y}_{jm}^{(m)}$, $\mathbf{Y}_{jm}^{(e)}$ and $\mathbf{Y}_{jm}^{(0)}$ are electric, magnetic and longitudinal harmonics, respectively; $\mathbf{e}_{\pm 1}(\hat{\mathbf{r}}) = \mp(\mathbf{e}_x(\hat{\mathbf{r}}) \pm i\mathbf{e}_y(\hat{\mathbf{r}}))/\sqrt{2}$; $\mathbf{e}_x(\hat{\mathbf{r}}) \equiv \mathbf{e}_\theta(\hat{\mathbf{r}}) = (\cos\theta \cos\phi, \cos\theta \sin\phi, -\sin\theta)$, $\mathbf{e}_y(\hat{\mathbf{r}}) \equiv \mathbf{e}_\phi(\hat{\mathbf{r}}) = (-\sin\phi, \cos\phi, 0)$ are the unit vectors tangential to the sphere; ϕ (θ) is the azimuthal (polar) angle of the unit vector $\hat{\mathbf{r}} = \mathbf{r}/r = (\sin\theta \cos\phi, \sin\theta \sin\phi, \cos\theta) \equiv \mathbf{e}_0(\hat{\mathbf{r}}) \equiv \mathbf{e}_z(\hat{\mathbf{r}})$; $f(\hat{\mathbf{r}}) \equiv f(\phi, \theta)$. (Hats will denote unit vectors and an asterisk will indicate complex conjugation.)

Note that, for the irreducible representation of the rotation group with the angular number j , the D -functions, $D_{m\nu}^j(\alpha, \beta, \gamma) = \exp(-im\alpha) d_{m\mu}^j(\beta) \exp(-i\mu\gamma)$, give the elements of

the rotation matrix parametrized by the three Euler angles [49, 50]: α , β and γ . In formulas (3) and throughout this paper, we assume that $\gamma = 0$ and $D_{m\nu}^j(\hat{\mathbf{r}}) \equiv D_{m\nu}^j(\phi, \theta, 0)$. Owing to the orthogonality relations for D -functions [49, 50], a set of vector spherical harmonics is orthonormal:

$$\langle \mathbf{Y}_{jm}^{(\alpha)*}(\hat{\mathbf{r}}) \cdot \mathbf{Y}_{j'm'}^{(\beta)}(\hat{\mathbf{r}}) \rangle_{\hat{\mathbf{r}}} = \delta_{\alpha\beta} \delta_{jj'} \delta_{mm'}. \quad (4)$$

where $\langle f \rangle_{\hat{\mathbf{r}}} \equiv \int_0^{2\pi} d\phi \int_0^\pi \sin\theta d\theta f(\hat{\mathbf{r}})$.

It can be shown [36] that the vector spherical harmonics (3) can also be recast into the well-known standard form [51]:

$$\mathbf{Y}_{jm}^{(m)}(\hat{\mathbf{r}}) = n_j \mathbf{L} Y_{jm} = -i\hat{\mathbf{r}} \times \mathbf{Y}_{jm}^{(e)}, \quad (5a)$$

$$\mathbf{Y}_{jm}^{(e)}(\hat{\mathbf{r}}) = n_j r \nabla Y_{jm} = -i\hat{\mathbf{r}} \times \mathbf{Y}_{jm}^{(m)}, \quad n_j \equiv [j(j+1)]^{-1/2}, \quad (5b)$$

where $Y_{jm}(\hat{\mathbf{r}}) \equiv Y_{jm}(\phi, \theta)$ is the normalized spherical function; $\mathbf{L} = -i\mathbf{r} \times \nabla$ is the operator of angular momentum

The vector wave functions, $\mathbf{M}_{jm}^{(\alpha)}$ and $\mathbf{N}_{jm}^{(\alpha)}$, are the solenoidal solutions of the vector Helmholtz equation that can be derived (a discussion of the procedure can be found, e.g., in Ref. [52]) from the solutions of the scalar Helmholtz equation taken in the factorized form: $\psi_{jm}^{(\alpha)} = n_j z_j^{(\alpha)}(kr) Y_{jm}(\hat{\mathbf{r}})$, where $z_j^{(\alpha)}(x)$ is either a spherical Bessel function, $j_j(x) = [\pi/(2x)]^{1/2} J_{j+1/2}(x)$, or a spherical Hankel function [53], $h_j^{(1,2)}(x) = [\pi/(2x)]^{1/2} H_{j+1/2}^{(1,2)}(x)$.

In the far-field region ($\rho \gg 1$), the asymptotic behavior of the spherical Bessel and Hankel functions is known [53]:

$$i^{j+1} h_j^{(1)}(\rho), i^j D h_j^{(1)}(\rho) \sim \exp(i\rho)/\rho, \quad (6a)$$

$$(-i)^{j+1} h_j^{(2)}(\rho), (-i)^j D h_j^{(2)}(\rho) \sim \exp(-i\rho)/\rho, \quad (6b)$$

$$i^{j+1} j_j(\rho), i^{j+1} D j_{j+1}(\rho) \sim [\exp(i\rho) - (-1)^j \exp(-i\rho)]/(2\rho). \quad (6c)$$

So, the spherical Hankel functions of the first kind, $h_j^{(1)}(\rho)$, describe the outgoing waves, whereas those of the second kind, $h_j^{(2)}(\rho)$, represent the incoming waves. For such waves, similar to Eqs. (2a)-(2b), the expansions in vector spherical harmonics can be written in terms of the vector wave functions: $\mathbf{M}_{jm}^{(1,2)}$ and $\mathbf{N}_{jm}^{(1,2)}$ given in Eqs. (2c) and (2d) with $z_j^{(1,2)} = h_j^{(1,2)}$. From the asymptotic relations (6a) and (6b), the vector wave functions of outgoing and incoming waves in the far-field region are given by

$$\mathbf{M}_{jm}^{(\text{out})} \equiv \mathbf{M}_{jm}^{(1)} \sim (-i)^{j+1} \frac{e^{i\rho}}{\rho} \mathbf{Y}_{jm}^{(m)}, \quad \mathbf{N}_{jm}^{(\text{out})} \equiv \mathbf{N}_{jm}^{(1)} \sim (-i)^j \frac{e^{i\rho}}{\rho} \mathbf{Y}_{jm}^{(e)}, \quad (7)$$

$$\mathbf{M}_{jm}^{(\text{in})} \equiv \mathbf{M}_{jm}^{(2)} \sim i^{j+1} \frac{e^{-i\rho}}{\rho} \mathbf{Y}_{jm}^{(m)}, \quad \mathbf{N}_{jm}^{(\text{in})} \equiv \mathbf{N}_{jm}^{(2)} \sim i^j \frac{e^{-i\rho}}{\rho} \mathbf{Y}_{jm}^{(e)}. \quad (8)$$

Thus outside the scatterer the optical field is a sum of the incident wave field with $z_j^{(\text{inc})}(\rho) = j_j(\rho) = [h_j^{(1)}(\rho) + h_j^{(2)}(\rho)]/2$ and the scattered waves with $z_j^{(\text{sca})}(\rho) = h_j^{(1)}(\rho)$ as required by the Sommerfeld radiation condition. The incident field is the field that would exist without a scatterer and therefore includes both incoming and outgoing parts (see Eq. (6c)) because, when no scattering, what comes in must go outwards again. As opposed

to the spherical Hankel functions that are singular at the origin, the incident wave field should be finite everywhere and thus is described by the regular Bessel functions $j_j(\rho)$.

Now the incident wave is characterized by amplitudes $\alpha_{jm}^{(\text{inc})}$, $\beta_{jm}^{(\text{inc})}$ and the scattered outgoing waves are similarly characterized by amplitudes $\alpha_{jm}^{(\text{sca})}$, $\beta_{jm}^{(\text{sca})}$. So long as the scattering problem is linear, the coefficients $\alpha_{jm}^{(\text{sca})}$ and $\beta_{jm}^{(\text{sca})}$ can be written as linear combinations of $\alpha_{jm}^{(\text{inc})}$ and $\beta_{jm}^{(\text{inc})}$:

$$\begin{aligned}\alpha_{jm}^{(\text{sca})} &= \sum_{j',m'} \left[T_{jm,j'm'}^{11} \alpha_{j'm'}^{(\text{inc})} + T_{jm,j'm'}^{12} \beta_{j'm'}^{(\text{inc})} \right], \\ \beta_{jm}^{(\text{sca})} &= \sum_{j',m'} \left[T_{jm,j'm'}^{21} \alpha_{j'm'}^{(\text{inc})} + T_{jm,j'm'}^{22} \beta_{j'm'}^{(\text{inc})} \right].\end{aligned}\quad (9)$$

These formulas define the elements of the T -matrix in the most general case.

In general, the scattering process mixes angular momenta [11]. The light scattering from uniformly anisotropic scatterers [14, 15, 54, 55] provides an example of such a scattering process. In simpler scattering processes, by contrast, such angular momentum mixing does not take place. For example, radial anisotropy keeps intact spherical symmetry of the scatterer [14, 17, 56]. The T -matrix of a spherically symmetric scatterer is diagonal over the angular momenta and the azimuthal numbers: $T_{jj',mm'}^{nn'} = \delta_{jj'} \delta_{mm'} T_j^{nn'}$.

In order to calculate the elements of T -matrix and the coefficients $\alpha_{jm}^{(p)}$ and $\beta_{jm}^{(p)}$, we need to use continuity of the tangential components of the electric and magnetic fields as boundary conditions at $r = R_p$ ($\rho = k_{\text{med}} R_p \equiv x$). So, the coefficients of the expansion for the wave field inside the scatterer, $\alpha_{jm}^{(p)}$ and $\beta_{jm}^{(p)}$, are expressed in terms of the coefficients describing the incident light as follows

$$\alpha_{jm}^{(p)} \equiv a_j^{(p)} \alpha_{jm}^{(\text{inc})} = \frac{-i \alpha_{jm}^{(\text{inc})}}{\mu^{-1} v_j(x) u_j'(nx) - n^{-1} v_j'(x) u_j(nx)}, \quad \mu = \mu_p / \mu_{\text{med}}, \quad (10)$$

$$\beta_{jm}^{(p)} \equiv b_j^{(p)} \beta_{jm}^{(\text{inc})} = \frac{-i \beta_{jm}^{(\text{inc})}}{n^{-1} v_j(x) u_j'(nx) - \mu^{-1} v_j'(x) u_j(nx)}, \quad n = n_p / n_{\text{med}}, \quad (11)$$

where $a_j^{(p)}$ and $b_j^{(p)}$ are the *internal field coefficients*; $x = k_{\text{med}} R_p$, $u_j(x) = x j_j(x)$ and $v_j(x) = x h_j^{(1)}(x)$. The similar result relating the scattered wave and the incident wave

$$\alpha_{jm}^{(\text{sca})} = T_j^{11} \alpha_{jm}^{(\text{inc})} = \frac{n^{-1} u_j'(x) u_j(nx) - \mu^{-1} u_j(x) u_j'(nx)}{\mu^{-1} v_j(x) u_j'(nx) - n^{-1} v_j'(x) u_j(nx)} \alpha_{jm}^{(\text{inc})}, \quad (12)$$

$$\beta_{jm}^{(\text{sca})} = T_j^{22} \beta_{jm}^{(\text{inc})} = \frac{\mu^{-1} u_j(x) u_j'(nx) - n^{-1} u_j'(x) u_j(nx)}{n^{-1} v_j(x) u_j'(nx) - \mu^{-1} v_j'(x) u_j(nx)} \beta_{jm}^{(\text{inc})}, \quad (13)$$

defines the T -matrix for the simplest case of a spherically symmetric scatterer. In addition, since the parity of electric and magnetic harmonics with respect to the spatial inversion $\hat{\mathbf{r}} \rightarrow -\hat{\mathbf{r}}$ ($\{\phi, \theta\} \rightarrow \{\phi + \pi, \pi - \theta\}$) is different

$$\mathbf{Y}_{jm}^{(m)}(-\hat{\mathbf{r}}) = (-1)^j \mathbf{Y}_{jm}^{(m)}(\hat{\mathbf{r}}), \quad \mathbf{Y}_{jm}^{(e)}(-\hat{\mathbf{r}}) = (-1)^{j+1} \mathbf{Y}_{jm}^{(e)}(\hat{\mathbf{r}}), \quad (14)$$

where $f(\hat{\mathbf{r}}) \equiv f(\phi, \theta)$ and $f(-\hat{\mathbf{r}}) \equiv f(\phi + \pi, \pi - \theta)$, they do not mix provided the mirror symmetry has not been broken. In this case the T -matrix is diagonal and $T_j^{12} = T_j^{21} = 0$. The diagonal elements $T_j^{11} \equiv a_j$ and $T_j^{22} \equiv b_j$ are also called the *Mie coefficients*.

III. FAR-FIELD MATCHING

Formulas (10)–(13) describe the wavefield both inside and outside the particle when the expansion for the incident light beam is known. In this section we, following Ref. [36], apply the far-field matching method to evaluate the beam shape coefficients. To this end, we introduce the vector angular distributions characterizing the wave field in the far-field region. The coefficients are then derived by matching the far-field distributions for the incident wave and the corresponding expansions over vector spherical harmonics.

A. Beam shape coefficients

Our first step is to examine asymptotic behavior of the total optical field, which is a sum of the incident and scattered wave fields, in the far-field region, $\rho \gg 1$. The electric and magnetic fields in this region can be separated into the incoming and the outgoing parts

$$\mathbf{E}_{\text{tot}} = \mathbf{E}_{\text{inc}} + \mathbf{E}_{\text{sca}} \sim \mathbf{E}_{\text{tot}}^{(\infty)} = \frac{1}{\rho} [\exp(i\rho)\mathbf{E}_{\text{out}}(\hat{\mathbf{r}}) + \exp(-i\rho)\mathbf{E}_{\text{in}}(\hat{\mathbf{r}})], \quad (15)$$

$$\mathbf{H}_{\text{tot}} = \mathbf{H}_{\text{inc}} + \mathbf{H}_{\text{sca}} \sim \mathbf{H}_{\text{tot}}^{(\infty)} = \frac{1}{\rho} [\exp(i\rho)\mathbf{H}_{\text{out}}(\hat{\mathbf{r}}) + \exp(-i\rho)\mathbf{H}_{\text{in}}(\hat{\mathbf{r}})] \quad (16)$$

described by the far-field angular distributions: $\{\mathbf{E}_{\text{in}}, \mathbf{H}_{\text{in}}\}$ and $\{\mathbf{E}_{\text{out}}, \mathbf{H}_{\text{out}}\}$. These far-field vector amplitudes are normal to $\hat{\mathbf{r}}$ and their basic properties can be summarized by the following relations [9]:

$$\mu/n \mathbf{H}_{\text{out}}(\hat{\mathbf{r}}) = \hat{\mathbf{r}} \times \mathbf{E}_{\text{out}}(\hat{\mathbf{r}}), \quad \mu/n \mathbf{H}_{\text{in}}(\hat{\mathbf{r}}) = -\hat{\mathbf{r}} \times \mathbf{E}_{\text{in}}(\hat{\mathbf{r}}), \quad (17)$$

$$\mathbf{E}_{\text{out}}(\hat{\mathbf{r}}) = \mathbf{E}_{\text{out}}^{(\text{inc})}(\hat{\mathbf{r}}) + \mathbf{E}_{\text{out}}^{(\text{sca})}(\hat{\mathbf{r}}) \perp \hat{\mathbf{r}}, \quad \mathbf{E}_{\text{in}}(\hat{\mathbf{r}}) = -\mathbf{E}_{\text{out}}^{(\text{inc})}(-\hat{\mathbf{r}}). \quad (18)$$

Formulas (15)–(18) explicitly show that, in the far-field region, the incident wave field is defined by the electric-field angular distribution of the outgoing wave: $\mathbf{E}_{\text{out}}^{(\text{inc})}(\hat{\mathbf{r}})$. When the incident electromagnetic wave is represented by a superposition of propagating plane waves of the form

$$\mathbf{E}_{\text{inc}}(\mathbf{r}) \equiv \mathbf{E}_{\text{inc}}(\rho, \hat{\mathbf{r}}) = \langle \exp(i\rho \hat{\mathbf{k}} \cdot \hat{\mathbf{r}}) \mathbf{E}_{\text{inc}}(\hat{\mathbf{k}}) \rangle_{\hat{\mathbf{k}}}, \quad \mathbf{E}_{\text{inc}}(\hat{\mathbf{k}}) = \sum_{\nu=\pm 1} E_{\nu}(\hat{\mathbf{k}}) \mathbf{e}_{\nu}(\hat{\mathbf{k}}), \quad (19)$$

where $\langle f \rangle_{\hat{\mathbf{k}}} \equiv \int_0^{2\pi} d\phi_k \int_0^{\pi} \sin \theta_k d\theta_k f$, the distribution $\mathbf{E}_{\text{out}}^{(\text{inc})}(\hat{\mathbf{r}})$ is determined by the vector amplitudes of the plane waves as follows

$$\mathbf{E}_{\text{out}}^{(\text{inc})}(\hat{\mathbf{r}}) = -2\pi i \mathbf{E}_{\text{inc}}(\hat{\mathbf{r}}) = E_{\theta}^{(\text{out})}(\hat{\mathbf{r}}) \mathbf{e}_{\theta}(\hat{\mathbf{r}}) + E_{\phi}^{(\text{out})}(\hat{\mathbf{r}}) \mathbf{e}_{\phi}(\hat{\mathbf{r}}), \quad (20)$$

whereas the incoming part of the incident wave is described by the far-field angular distribution $\mathbf{E}_{\text{in}}^{(\text{inc})}(\hat{\mathbf{r}}) = -\mathbf{E}_{\text{out}}^{(\text{inc})}(-\hat{\mathbf{r}})$.

An important consequence of Eqs. (19) and (20) is that, translation of the wave fields

$$\{\mathbf{E}_{\text{inc}}(\mathbf{r}), \mathbf{H}_{\text{inc}}(\mathbf{r})\} \rightarrow \{\mathbf{E}_{\text{inc}}(\mathbf{r} + \mathbf{r}_p), \mathbf{H}_{\text{inc}}(\mathbf{r} + \mathbf{r}_p)\} \quad (21)$$

affects the far-field angular distribution (20) by producing the phase shift

$$\mathbf{E}_{\text{out}}^{(\text{inc})}(\hat{\mathbf{r}}) \rightarrow \mathbf{E}_{\text{out}}^{(\text{inc})}(\hat{\mathbf{r}}, \mathbf{r}_p) = \mathbf{E}_{\text{out}}^{(\text{inc})}(\hat{\mathbf{r}}) \exp[ik(\mathbf{r}_p \cdot \hat{\mathbf{r}})]. \quad (22)$$

Referring to Fig. 1, the vector $-\mathbf{r}_p$ will determine location of the beam waist with respect to the center of the particle.

The far-field distribution of an incident light beam, $\mathbf{E}_{\text{out}}^{(\text{inc})}(\hat{\mathbf{r}})$, can also be found from the expansion over the vector spherical harmonics (2a). The far-field asymptotics for the vector wave functions that enter the expansion for the incident wave (2)

$$\mathbf{M}_{jm}^{(\text{inc})}(\rho, \hat{\mathbf{r}}) \sim \frac{(-i)^{j+1}}{2\rho} [\exp(i\rho)\mathbf{Y}_{jm}^{(m)}(\hat{\mathbf{r}}) - \exp(-i\rho)\mathbf{Y}_{jm}^{(m)}(-\hat{\mathbf{r}})], \quad (23)$$

$$\mathbf{N}_{jm}^{(\text{inc})}(\rho, \hat{\mathbf{r}}) \sim \frac{(-i)^j}{2\rho} [\exp(i\rho)\mathbf{Y}_{jm}^{(e)}(\hat{\mathbf{r}}) - \exp(-i\rho)\mathbf{Y}_{jm}^{(e)}(-\hat{\mathbf{r}})], \quad (24)$$

can be derived from Eqs. (2c)-(2d) with the help of the far-field relation (6c). Substituting Eqs. (23) and (24) into Eq. (2a) gives the expansion for the far-field distribution (20)

$$\mathbf{E}_{\text{out}}^{(\text{inc})}(\hat{\mathbf{r}}) = 2^{-1} \sum_{jm} (-i)^{j+1} [\alpha_{jm}^{(\text{inc})} \mathbf{Y}_{jm}^{(m)}(\hat{\mathbf{r}}) + i\beta_{jm}^{(\text{inc})} \mathbf{Y}_{jm}^{(e)}(\hat{\mathbf{r}})] \equiv \sum_{jm} \sum_{\alpha \in \{e,m\}} w_{jm}^{(\alpha)} \mathbf{Y}_{jm}^{(\alpha)}, \quad (25)$$

where $w_{jm}^{(m)} = (-i)^{j+1} \alpha_{jm}^{(\text{inc})} / 2$ and $w_{jm}^{(e)} = (-i)^j \beta_{jm}^{(\text{inc})} / 2$. Similar result for the far-field angular distribution of the scattered wave, $\mathbf{E}_{\text{out}}^{(\text{sca})}(\hat{\mathbf{r}})$, is given by

$$\mathbf{E}_{\text{out}}^{(\text{sca})}(\hat{\mathbf{r}}) = \sum_{jm} (-i)^{j+1} [\alpha_{jm}^{(\text{sca})} \mathbf{Y}_{jm}^{(m)}(\hat{\mathbf{r}}) + i\beta_{jm}^{(\text{sca})} \mathbf{Y}_{jm}^{(e)}(\hat{\mathbf{r}})] \equiv \sum_{jm} \sum_{\alpha \in \{e,m\}} s_{jm}^{(\alpha)} \mathbf{Y}_{jm}^{(\alpha)}, \quad (26)$$

where $s_{jm}^{(m)} = (-i)^{j+1} \alpha_{jm}^{(\text{sca})}$ and $s_{jm}^{(e)} = (-i)^j \beta_{jm}^{(\text{sca})}$.

The coefficients of the incident wave can now be easily found as the Fourier coefficients of the far-field angular distribution, $\mathbf{E}_{\text{out}}^{(\text{inc})}$, expanded using the vector spherical harmonics basis (3). The final result reads

$$\begin{aligned} \alpha_{jm}^{(\text{inc})} &= 2i^{j+1} \langle \mathbf{Y}_{jm}^{(m)*}(\hat{\mathbf{r}}) \cdot \mathbf{E}_{\text{out}}^{(\text{inc})}(\hat{\mathbf{r}}) \rangle_{\hat{\mathbf{r}}} = 2n_j i^{j+1} \langle Y_{jm}^*(\hat{\mathbf{r}}) (\mathbf{L} \cdot \mathbf{E}_{\text{out}}^{(\text{inc})}(\hat{\mathbf{r}})) \rangle_{\hat{\mathbf{r}}} = \\ &2n_j i^j \int_0^{2\pi} d\phi \int_0^\pi d\theta Y_{jm}^*(\phi, \theta) \left[\partial_\theta (\sin \theta E_\phi^{(\text{out})}) - \partial_\phi E_\theta^{(\text{out})} \right], \end{aligned} \quad (27a)$$

$$\begin{aligned} \beta_{jm}^{(\text{inc})} &= 2i^j \langle \mathbf{Y}_{jm}^{(e)*}(\hat{\mathbf{r}}) \cdot \mathbf{E}_{\text{out}}^{(\text{inc})}(\hat{\mathbf{r}}) \rangle_{\hat{\mathbf{r}}} = -2n_j i^j \langle Y_{jm}^*(\hat{\mathbf{r}}) (r \nabla \cdot \mathbf{E}_{\text{out}}^{(\text{inc})}(\hat{\mathbf{r}})) \rangle_{\hat{\mathbf{r}}} = \\ &-2n_j i^j \int_0^{2\pi} d\phi \int_0^\pi d\theta Y_{jm}^*(\phi, \theta) \left[\partial_\theta (\sin \theta E_\theta^{(\text{out})}) + \partial_\phi E_\phi^{(\text{out})} \right], \end{aligned} \quad (27b)$$

where we have used Eqs. (5a) and (5b) to obtain the explicit analytical expressions useful for computational purposes.

B. Remodelled Laguerre–Gaussian beams

In the paraxial approximation, the LG beams are described in terms of scalar fields of the form: $u_{nm}(\mathbf{r}) \exp(ikz)$, where n (m) is the radial (azimuthal) mode number and $u_{nm}(\mathbf{r})$ is the solution of the paraxial Helmholtz equation that can be conveniently written in the cylindrical coordinate system, (r_\perp, ϕ, z) , as follows

$$u_{nm}(r_\perp, \phi, z) = |\sigma|^{-1} \psi_{nm}(\sqrt{2}r_\perp/w) \exp\{-r_\perp^2/(w_0^2\sigma) + im\phi - i\gamma_{nm}\}, \quad (28a)$$

$$\sigma \equiv \sigma(z) = 1 + iz/z_R, \quad w \equiv w(z) = w_0|\sigma|, \quad (28b)$$

$$\gamma_{nm} \equiv \gamma_{nm}(z) = (2n + m + 1) \arctan(z/z_R), \quad \psi_{nm}(x) = x^{|m|} L_n^{|m|}(x^2), \quad (28c)$$

where L_n^m is the generalized Laguerre polynomial given by [57]

$$L_n^m(x) = (n!)^{-1} x^{-m} \exp(x) \partial_x^n [x^{n+m} \exp(-x)], \quad (29)$$

w_0 is the initial transverse Gaussian half-width (the beam diameter at waist) $z_R = kw_0^2/2 = [2kf^2]^{-1}$ is the Rayleigh range and $f = [kw_0]^{-1}$ is the *focusing parameter*.

The problem studied in Refs. [30, 32, 33] deals with the exact propagation of the optical field in the half-space, $z > 0$, when its transverse components at the initial (source) plane, $z = 0$, are known. In Ref. [32], the results describing asymptotic behavior of the linearly polarized field

$$\mathbf{E}(r_\perp, \phi, 0) = u_{nm}(r_\perp, \phi, 0) \hat{\mathbf{x}} = \psi_{nm}(\sqrt{2}r_\perp/w_0) \exp\{-r_\perp^2/w_0^2 + im\phi\} \hat{\mathbf{x}} \quad (30)$$

were derived using the angular spectrum representation (Debye integrals) and comply with both the results of rigorous mathematical analysis performed in Ref. [58] and those obtained using the vectorial Rayleigh-Sommerfeld integrals [30, 33]. The resulting expression for the far-field angular distribution can be written in the following form

$$\mathbf{E}_{\text{out}}^{(\text{LG})}(\phi, \theta) = E_{nm}(f^{-1} \sin \theta / \sqrt{2}) \exp(im\phi) \mathbf{e}_{\text{out}}, \quad (31a)$$

$$\mathbf{e}_{\text{out}} = \cos \phi \mathbf{e}_\theta(\hat{\mathbf{r}}) - \cos \theta \sin \phi \mathbf{e}_\phi(\hat{\mathbf{r}}) = \cos \theta \hat{\mathbf{x}} - \sin \theta \cos \phi \hat{\mathbf{z}}, \quad (31b)$$

$$E_{nm}(x) = \frac{x^m}{i^{2n+m+1} 2 f^2} L_n^m(x^2) \exp(-x^2/2). \quad (31c)$$

The beam shape coefficients for the LG beams can now be computed from formulas (27) where the far-field distribution $\mathbf{E}_{\text{out}}^{(\text{inc})}$ is defined in Eq. (31a). We can also combine the relations (20) and (19) with the outgoing part of the far-field distribution (31a) to deduce the expression for the electric field of the remodelled LG beam

$$\begin{aligned} \mathbf{E}_{\text{inc}}^{(\text{LG})}(\rho_\perp, \phi, \rho_z) &= E_x^{(\text{LG})}(\rho_\perp, \phi, \rho_z) \hat{\mathbf{x}} + E_z^{(\text{LG})}(\rho_\perp, \phi, \rho_z) \hat{\mathbf{z}} = \\ &= \frac{i}{2\pi} \langle \exp [i(\rho_\perp \sin \theta_k \cos(\phi - \phi_k) + \rho_z \cos \theta_k)] \mathbf{E}_{\text{out}}^{(\text{LG})}(\hat{\mathbf{k}}) \rangle_{\hat{\mathbf{k}}}, \end{aligned} \quad (32)$$

where $\rho_\perp = kr_\perp$ and $\rho_z = kz$.

IV. OPTICAL FORCE AND SYMMETRIES

The electric-field far-field distributions for the incident and the scattered waves (see Eqs (25) and (26), respectively) are found to play a major part in the method of far-field matching. In particular, they determine the beam shape coefficients (27) and incorporate dependence on the particle position [see Eq. (22)]. In this section, we derive a useful far-field expression for the optical force and discuss some symmetry properties of the LG beams.

A. Maxwell's stress tensor and optical force

It is not difficult to obtain the far-field expression for the time-averaged Poynting vector of the total wavefield given in Eqs. (15)–(17) $\mathbf{S}_{\text{tot}} = c/(8\pi) \text{Re}(\mathbf{E}_{\text{tot}} \times \mathbf{H}_{\text{tot}}^*)$

$$\mathbf{S}_{\text{tot}}(\rho, \hat{\mathbf{r}}) \sim \mathbf{S}_{\text{tot}}^{(\infty)}(\rho, \hat{\mathbf{r}}) = \frac{cn}{8\pi\mu\rho^2} \left\{ |\mathbf{E}_{\text{out}}(\hat{\mathbf{r}})|^2 - |\mathbf{E}_{\text{in}}(\hat{\mathbf{r}})|^2 \right\} \hat{\mathbf{r}} \quad (33)$$

where $|\mathbf{E}_\alpha(\hat{\mathbf{r}})|^2 = (\mathbf{E}_\alpha(\hat{\mathbf{r}}) \cdot \mathbf{E}_\alpha^*(\hat{\mathbf{r}}))$, and use the relations (18) to evaluate the flux of the Poynting vector (33) through the far-field sphere S_f of the radius R_f .

The result can be written in the following well-known form:

$$\oint_{S_f} (\mathbf{S}_{\text{tot}}^{(\infty)} \cdot d\mathbf{s}) = R_f^2 \langle (\mathbf{S}_{\text{tot}}^{(\infty)}(kR_f, \hat{\mathbf{r}}) \cdot \hat{\mathbf{r}}) \rangle_{\hat{\mathbf{r}}} \equiv -W_{\text{abs}} = W_{\text{sca}} - W_{\text{ext}}, \quad (34)$$

$$W_{\text{sca}} = \frac{cn}{8\pi\mu k^2} \langle |\mathbf{E}_{\text{out}}^{(\text{sca})}(\hat{\mathbf{r}})|^2 \rangle_{\hat{\mathbf{r}}}, \quad W_{\text{ext}} = -\frac{cn}{4\pi\mu k^2} \text{Re} \langle (\mathbf{E}_{\text{out}}^{(\text{sca})}(\hat{\mathbf{r}}) \cdot [\mathbf{E}_{\text{out}}^{(\text{inc})}(\hat{\mathbf{r}})]^*) \rangle_{\hat{\mathbf{r}}}, \quad (35)$$

where W_{sca} is the energy scattering rate (the rate at which the scattered energy crosses the sphere in the outward direction), W_{abs} is the energy absorption rate and $W_{\text{ext}} = W_{\text{sca}} + W_{\text{abs}}$ is the extinction rate. When the scatterer and the surrounding medium are both non-absorbing, the energy absorption rate vanishes, $W_{\text{abs}} = 0$, and Eq. (34) yields unitarity relations for the T -matrix [9] (see also Eq. (A3) in Appendix A). In our spherically symmetric case, these are: $|2T_j^{11} + 1|^2 = |2T_j^{22} + 1|^2 = 1$.

According to Ref. [42], the total power of the incident laser beam, W_{inc} , can be computed by integrating the Poynting vector for the outgoing part of the incident field. In our case, this part expressed in terms of the beam shape coefficients is given in Eq. (25) and the total power of the incident beam can be written in the form of a sum:

$$W_{\text{inc}} = \frac{cn}{8\pi\mu k^2} \langle |\mathbf{E}_{\text{out}}^{(\text{inc})}(\hat{\mathbf{r}})|^2 \rangle_{\hat{\mathbf{r}}} = \sum_j \{W_j^{(m)} + W_j^{(e)}\}, \quad (36)$$

where $W_j^{(m)}$ ($W_j^{(e)}$) is the power of magnetic (electric) modes with the angular momentum j given by

$$W_j^{(m)} = \frac{cn}{32\pi\mu k^2} \sum_{m=-j}^j |\alpha_{jm}^{(\text{inc})}|^2, \quad W_j^{(e)} = \frac{cn}{32\pi\mu k^2} \sum_{m=-j}^j |\beta_{jm}^{(\text{inc})}|^2. \quad (37)$$

The far-field angular distributions, $\mathbf{E}_{\text{out}}^{(\text{sca})}(\hat{\mathbf{r}})$ and $\mathbf{E}_{\text{out}}^{(\text{inc})}(\hat{\mathbf{r}})$, also determine the time-averaged optical force, \mathbf{F} , acting upon the particle. This force can be expressed in terms of the time-average of Maxwell's stress tensor \mathbf{T}_M

$$\mathbf{T}_M = \frac{1}{8\pi} \text{Re} \{ \epsilon \mathbf{E} \otimes \mathbf{E}^* + \mu \mathbf{H} \otimes \mathbf{H}^* - \mathbf{I}(\epsilon |\mathbf{E}|^2 + \mu |\mathbf{H}|^2)/2 \}, \quad (38)$$

where \mathbf{I} is the unit dyadic, as follows:

$$\mathbf{F} = \oint_{S_f} (\mathbf{T}_M^{(\infty)} \cdot d\mathbf{s}), \quad (39)$$

where $\mathbf{T}_M^{(\infty)}$ is the Maxwell stress tensor (38) in the far-field region. Substituting Eqs. (15)–(17) into the stress tensor (38) gives the following expression for the dot product

$$(\mathbf{T}_M^{(\infty)} \cdot \hat{\mathbf{r}}) = -\frac{\epsilon}{8\pi\rho^2} \left\{ |\mathbf{E}_{\text{out}}(\hat{\mathbf{r}})|^2 + |\mathbf{E}_{\text{in}}(\hat{\mathbf{r}})|^2 \right\} \hat{\mathbf{r}} \quad (40)$$

that enter the integrand on the right-hand side of Eq. (39). The resulting expression for the optical force is

$$\mathbf{F}(\mathbf{r}_p) = -\frac{\epsilon}{8\pi k^2} \left\{ \langle \hat{\mathbf{r}} | \mathbf{E}_{\text{out}}^{(\text{sca})}(\hat{\mathbf{r}}, \mathbf{r}_p) |^2 \rangle_{\hat{\mathbf{r}}} + 2 \operatorname{Re} \langle \hat{\mathbf{r}} | [\mathbf{E}_{\text{out}}^{(\text{inc})}(\hat{\mathbf{r}}, \mathbf{r}_p)]^* \cdot \mathbf{E}_{\text{out}}^{(\text{sca})}(\hat{\mathbf{r}}, \mathbf{r}_p) \rangle_{\hat{\mathbf{r}}} \right\}, \quad (41)$$

where we have indicated that the net force exerted on the particle depends on the displacement vector \mathbf{r}_p describing position of the scatterer with respect to the focal plane (see Fig. 1).

In the special case of plane-wave illumination, the far-field expression for the optical force was derived in Ref. [59]. In Appendix A we show that formula (41) can alternatively be recast into the form (see Eq. (A9)) where the terms containing derivatives with respect to coordinates of the displacement vector \mathbf{r}_p (the gradient terms) are explicitly separated out.

In the spherical basis, $\hat{\mathbf{e}}_{\pm} = \mp(\hat{\mathbf{x}} \pm i\hat{\mathbf{y}})/\sqrt{2}$ and $\hat{\mathbf{e}}_0 = \hat{\mathbf{z}}$, the components of the optical force can be expressed in terms of the coefficients that enter the expansions for the incident and scattered waves [see Eqs. (25) and (26)] as follows

$$F_{\nu} = (\mathbf{F} \cdot \hat{\mathbf{e}}_{\nu}^*) = -\frac{\epsilon}{8\pi k^2} \sum_{jm} \sum_{j'm'} \left\{ p_{mm'}^{jj'} P_{mm'\nu}^{jj'1} + q_{mm'}^{jj'} Q_{mm'\nu}^{jj'1} \right\} \quad (42)$$

$$p_{mm'}^{jj'} = \sum_{\alpha} \left\{ s_{jm}^{(\alpha)} s_{j'm'}^{(\alpha)*} + s_{jm}^{(\alpha)} w_{j'm'}^{(\alpha)*} + w_{jm}^{(\alpha)} s_{j'm'}^{(\alpha)*} \right\} \quad (43)$$

$$q_{mm'}^{jj'} = \sum_{\alpha, \beta} (1 - \delta_{\alpha\beta}) \left\{ s_{jm}^{(\alpha)} s_{j'm'}^{(\beta)*} + s_{jm}^{(\alpha)} w_{j'm'}^{(\beta)*} + w_{jm}^{(\alpha)} s_{j'm'}^{(\beta)*} \right\}, \quad (44)$$

$$\begin{aligned} P_{mm'\nu}^{jj'1} &= N_j N_{j'}/2 \sum_{\mu=\pm 1} \langle D_{m\mu}^{j*}(\hat{\mathbf{r}}) D_{m'\mu}^{j'}(\hat{\mathbf{r}}) D_{\nu 0}^1(\hat{\mathbf{r}}) \rangle_{\hat{\mathbf{r}}} \\ &= \frac{1}{8} \sqrt{\frac{2j'+1}{2j+1}} C_{\nu m' m}^{1j'j} \sum_{\mu=\pm 1} C_{0\mu\mu}^{1j'j}, \end{aligned} \quad (45)$$

$$\begin{aligned} Q_{mm'\nu}^{jj'1} &= -N_j N_{j'}/2 \sum_{\mu=\pm 1} \mu \langle D_{m\mu}^{j*}(\hat{\mathbf{r}}) D_{m'\mu}^{j'}(\hat{\mathbf{r}}) D_{\nu 0}^1(\hat{\mathbf{r}}) \rangle_{\hat{\mathbf{r}}} \\ &= -\frac{1}{8} \sqrt{\frac{2j'+1}{2j+1}} C_{\nu m' m}^{1j'j} \sum_{\mu=\pm 1} \mu C_{0\mu\mu}^{1j'j}, \end{aligned} \quad (46)$$

where $\nu \in \{\pm 1, 0\}$ and $C_{\nu m' m}^{1j'j}$ denotes the Clebsch-Gordon (Wigner) coefficient. Derivation of formula (42) involves the following steps: (a) substituting expansions (25) and (26) into the expression for the optical force; (b) using the components of the vector $\hat{\mathbf{r}}$ expressed in terms of D functions: $(\hat{\mathbf{r}} \cdot \hat{\mathbf{e}}_{\nu}^*) = D_{\nu 0}^1(\hat{\mathbf{r}})$; (c) using Eq. (3) to compute dot products of the vector spherical functions $(\mathbf{Y}_{jm}^{(\alpha)} \cdot \mathbf{Y}_{j'm'}^{(\beta)*})$ and (d) using the relation [49]

$$\langle D_{m\mu}^{j*}(\hat{\mathbf{r}}) D_{m'\mu}^{j'}(\hat{\mathbf{r}}) D_{\nu 0}^1(\hat{\mathbf{r}}) \rangle_{\hat{\mathbf{r}}} = \frac{\pi}{2j+1} C_{\nu m' m}^{1j'j} C_{0\mu\mu}^{1j'j} \quad (47)$$

to perform the integrals.

The result (42) can be further simplified by using the permutation symmetry relations

$$p_{m'm}^{j'j} = [p_{mm'}^{jj'}]^*, \quad q_{m'm}^{j'j} = [q_{mm'}^{jj'}]^*, \quad (48)$$

$$P_{m'\nu}^{j'j1} = (-1)^{\nu} P_{mm'-\nu}^{jj'1}, \quad Q_{m'\nu}^{j'j1} = (-1)^{\nu} Q_{mm'-\nu}^{jj'1} \quad (49)$$

and the explicit expressions for the coefficients

$$P_{mm'\nu}^{jj1} = 0, \quad Q_{mm'\nu}^{jj1} = -\frac{\delta_{m', m-\nu}}{4j(j+1)} \begin{cases} m, & \nu = 0 \\ [(j+\nu m)(j-\nu m+1)/2]^{1/2}, & \nu = \pm 1 \end{cases} \quad (50)$$

$$Q_{mm'\nu}^{j-1j1} = 0, \quad P_{mm'\nu}^{j-1j1} = \frac{\delta_{m', m-\nu}}{4j} \sqrt{\frac{j^2-1}{4j^2-1}} \begin{cases} [j^2-m^2]^{1/2}, & \nu = 0 \\ [(j-\nu m)(j-\nu m+1)/2]^{1/2}, & \nu = \pm 1 \end{cases} \quad (51)$$

derived with the help of formulas for the Clebsch-Gordon coefficients (see, e.g., the table on pg. 635 of the book [49]).

The final result for the components of the optical force (41) reads

$$F_\nu = -\frac{\epsilon}{8\pi k^2} \sum_{jm} \left\{ q_{mm-\nu}^{jj} Q_{mm-\nu\nu}^{jj1} + [q_{mm-\nu}^{jj}]^* (-1)^\nu Q_{mm+\nu-\nu}^{jj1} \right. \\ \left. + p_{mm-\nu}^{j-1j} P_{mm-\nu\nu}^{j-1j1} + [p_{mm-\nu}^{j-1j}]^* (-1)^\nu P_{mm+\nu-\nu}^{j-1j1} \right\}. \quad (52)$$

Note that it is often useful to rescale the force by introducing the dimensionless force efficiency [4]

$$\mathbf{F}_{\text{eff}} = \mathbf{F}/F_{\text{scl}}, \quad F_{\text{scl}} = nW_{\text{inc}}/c, \quad (53)$$

where F_{scl} is the force scale factor proportional to the power of the incident beam W_{inc} given by Eq. (36).

B. Symmetries of laser beams and stiffness matrix

In Sec. IV A, we have shown that the scattering characteristics such as the cross-sections and the radiation force can be expressed in terms of the far-field angular distributions that can be regarded as vector fields on a sphere. Under the action of the orthogonal transformation $M: \hat{\mathbf{r}} \mapsto \hat{\mathbf{r}}' = M\hat{\mathbf{r}}$ such fields transform as follows:

$$\mathbf{E}_{\text{out}}(\hat{\mathbf{r}}) \mapsto \mathbf{E}'_{\text{out}} = M\mathbf{E}_{\text{out}}(M^{-1}\hat{\mathbf{r}}). \quad (54)$$

From Eqs. (19) and (41) we derive the relations

$$\mathbf{E}_{\text{inc}}(\mathbf{r}) \mapsto \mathbf{E}'_{\text{inc}} = M\mathbf{E}_{\text{inc}}(M^{-1}\mathbf{r}), \quad \mathbf{F}[\mathbf{E}_{\text{out}}] \mapsto \mathbf{F}[\mathbf{E}'_{\text{out}}] = M\mathbf{F}[\mathbf{E}_{\text{out}}] \quad (55)$$

that define transformations of the incident wave and the optical force.

The symmetry transformation M_s for the far-field angular distribution of the incident wave may generally be defined through the symmetry relation

$$M_s \mathbf{E}_{\text{out}}^{(\text{inc})}(M_s^{-1}\hat{\mathbf{r}}) = p_s \mathbf{E}_{\text{out}}^{(\text{inc})}(\hat{\mathbf{r}}), \quad (56)$$

where $p_s \equiv \exp(i\psi_s)$ is the phase factor. At $|\mathbf{r}_p| \neq 0$, we can use Eq. (22) combined with the orthogonality relation: $(\hat{\mathbf{r}} \cdot \mathbf{r}_p) = (M_s^{-1}\hat{\mathbf{r}} \cdot M_s^{-1}\mathbf{r}_p)$ to recast the symmetry condition (56) in the form:

$$p_s \mathbf{E}_{\text{out}}^{(\text{inc})}(\hat{\mathbf{r}}, \mathbf{r}_p) = M_s \mathbf{E}_{\text{out}}^{(\text{inc})}(M_s^{-1}\hat{\mathbf{r}}, M_s^{-1}\mathbf{r}_p). \quad (57)$$

As a direct consequence of the generalized symmetry relation (57) for the optical force we have

$$\mathbf{F}(\mathbf{r}_p) = M_s \mathbf{F}(M_s^{-1} \mathbf{r}_p), \quad \mathbf{K}(\mathbf{r}_p) = M_s \mathbf{K}(M_s^{-1} \mathbf{r}_p) M_s^{-1}, \quad (58)$$

where the elements of the stiffness (force) matrix $\mathbf{K}(\mathbf{r}_p)$ are given by

$$K_{ij}(\mathbf{r}_p) = \partial_j F_i(\mathbf{r}_p). \quad (59)$$

At equilibria, the force vanishes ($\mathbf{F}(\mathbf{r}_{\text{eq}}) = \mathbf{0}$) and the stiffness matrix, $\mathbf{K}_{\text{eq}} = \mathbf{K}(\mathbf{r}_{\text{eq}})$, is known to govern the regime of linearized dynamics of the particle [44].

For the LG beams with the angular distribution (31a), it can be easily checked that the direction of propagation (the z axis) is the axis of twofold rotational symmetry C_2 with $C_2 : \phi \mapsto \phi + \pi$ and $C_2 = \text{diag}(-1, -1, 1)$. From Eq. (31a), we have

$$C_2 \mathbf{E}_{\text{out}}^{(\text{LG})}(C_2 \hat{\mathbf{r}}) = C_2 \mathbf{E}_{\text{out}}^{(\text{LG})}(\phi + \pi, \theta) = (-1)^{m+1} \mathbf{E}_{\text{out}}^{(\text{LG})}(\hat{\mathbf{r}}). \quad (60)$$

When $\mathbf{r}_p \parallel \hat{\mathbf{z}}$ and $C_2 \mathbf{r}_p = \mathbf{r}_p$, equation (58) for the twofold symmetry implies that the optical force is directed along the symmetry axis, $\mathbf{F} \parallel \hat{\mathbf{z}}$, and the stiffness matrix is of the form:

$$\mathbf{K} = \begin{pmatrix} K_{xx} & K_{xy} & 0 \\ K_{yx} & K_{yy} & 0 \\ 0 & 0 & K_{zz} \end{pmatrix}. \quad (61)$$

Since $C_2 \mathbf{Y}_{jm}^{(e,m)}(C_2 \hat{\mathbf{r}}) = (-1)^m \mathbf{Y}_{jm}^{(e,m)}(\hat{\mathbf{r}})$, for C_2 symmetric LG beams, the azimuthal numbers of nonvanishing beam shape coefficients are of the same parity (all m are either odd or even).

We conclude this section with the remark on the special case of non-vortex LG beams with the vanishing azimuthal mode number. At $m = 0$, the angular distribution (31a) is invariant under the reflection

$$\sigma_{xz} \mathbf{E}_{\text{out}}^{(\text{LG})}(\sigma_{xz} \hat{\mathbf{r}}) = \sigma_{xz} \mathbf{E}_{\text{out}}^{(\text{LG})}(-\phi, \theta) = \mathbf{E}_{\text{out}}^{(\text{LG})}(\hat{\mathbf{r}}), \quad (62)$$

where $\sigma_{xz} = \text{diag}(1, -1, 1)$. This mirror plane symmetry places additional constraints on the elements of the stiffness matrix at $\mathbf{r}_d = \sigma_{xz} \mathbf{r}_d$. From Eq. (58), it can be inferred that the non-diagonal elements K_{xy} and K_{yx} should be equal to zero. So, for non-vortex beams with $m = 0$, the matrix (61) is diagonal

$$\mathbf{K} = \text{diag}(K_{xx}, K_{yy}, K_{zz}). \quad (63)$$

V. RESULTS

In this section, we present the results of numerical computations on the radiation force (41) for the case where the incident wave is represented by the remodelled LG beams (32) with the radial mode number $n = n_{\text{LG}} \in \{0, 1\}$ and the azimuthal number, $m = m_{\text{LG}} \in \{0, 1, 2\}$. Substituting the far-field distribution (31) into Eq. (27) gives the beam shape coefficients of these beams in the form that agrees with our symmetry analysis:

$$\alpha_{jm}^{(\text{inc})} = \alpha_{j, m_{\text{LG}}}^{(+)} \delta_{m, m_{\text{LG}}+1} + \alpha_{j, m_{\text{LG}}}^{(-)} \delta_{m, m_{\text{LG}}-1}, \quad (64a)$$

$$\beta_{jm}^{(\text{inc})} = \beta_{j, m_{\text{LG}}}^{(+)} \delta_{m, m_{\text{LG}}+1} + \beta_{j, m_{\text{LG}}}^{(-)} \delta_{m, m_{\text{LG}}-1}. \quad (64b)$$

Then the coefficients of expansions (2) describing scattered wave and electromagnetic field inside the scatterer can be evaluated from formulas (10)–(13). These coefficients enter the expression for the components of the optical force (52). The optical-force-induced dynamics of the particle will be of our primary concern.

A. Linearized dynamics and stability of equilibria

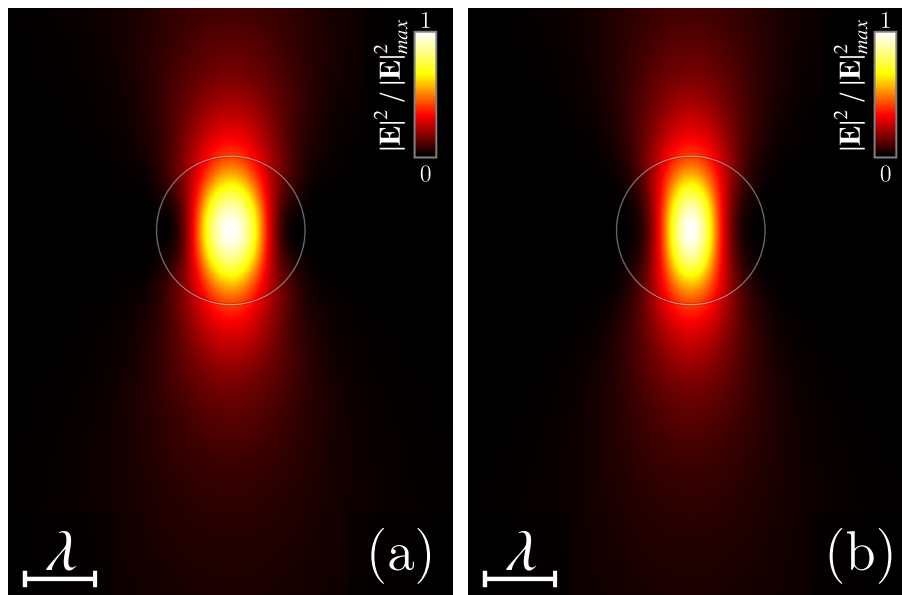


Figure 2: (Color online) Intensity distributions of the incident wave field in (a) the $x - z$ plane and (b) the $y - z$ plane for the LG_{00} (Gaussian) beam with $n_{\text{LG}} = m_{\text{LG}} = 0$ and $f = 0.3$. The z axis is directed from the top down.

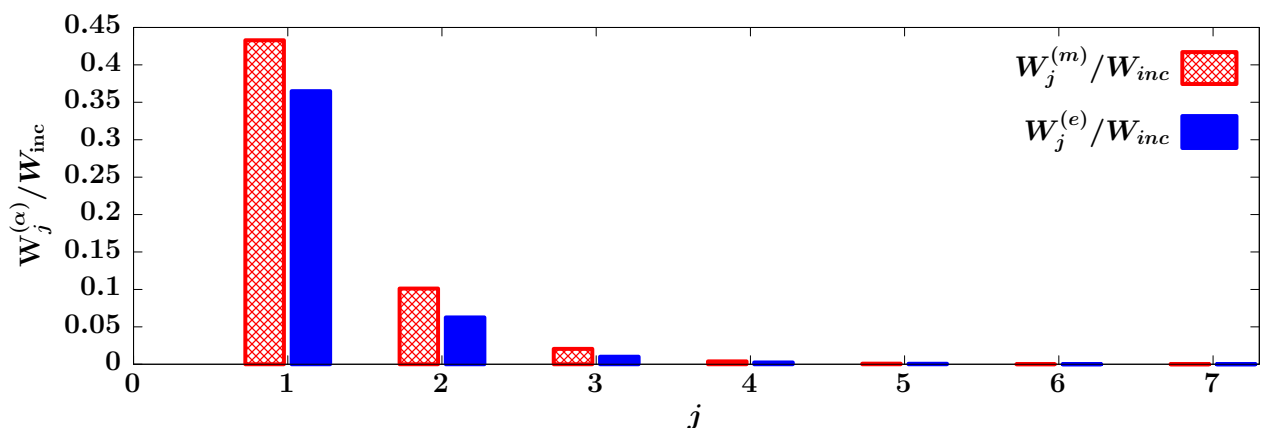


Figure 3: (Color online) Histogram of multipolar decomposition of the incident LG_{00} (Gaussian) beam with $f = 0.3$. Height of the bars represents relative contribution of the modes, $W_j^{(m)} / W_{\text{inc}}$ and $W_j^{(e)} / W_{\text{inc}}$, (see Eqs. (36) and (37)) to the total power of the incident beam depending on the angular momentum number j .

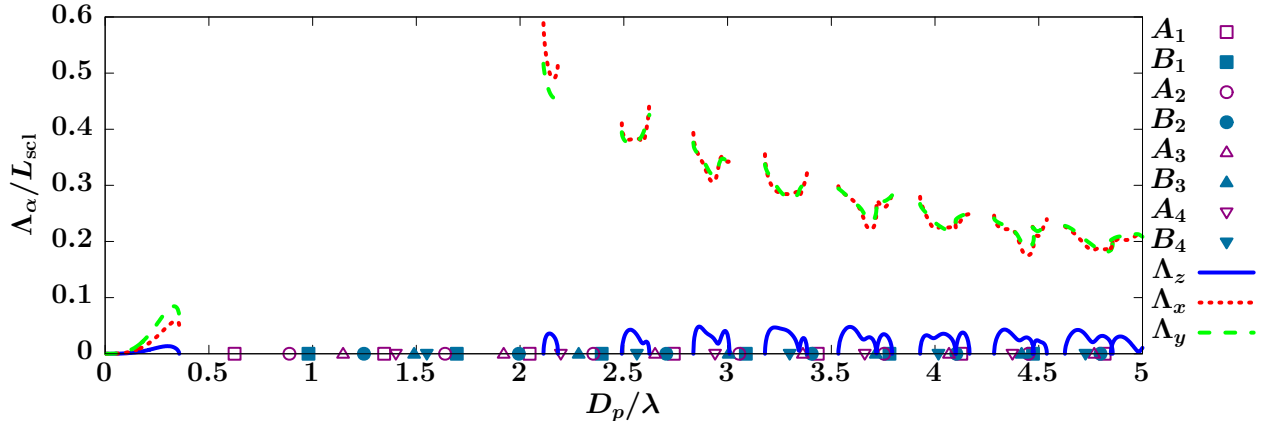


Figure 4: (Color online) Eigenvalues of the effective stiffness matrix \mathbf{L}_{eff} (see Eqs. (72) and (73)), $\Lambda_\alpha/L_{\text{scl}}$, as a function of the size parameter, $D_p/\lambda = 2R_p/\lambda$, for the LG₀₀ beam with $f = 0.3$. The scale factor is $L_{\text{scl}} = nW_{\text{inc}}/(c\lambda m_p)$ (see Eq. (72)) and the refractive index of the particle is $n_p = 1.33$.

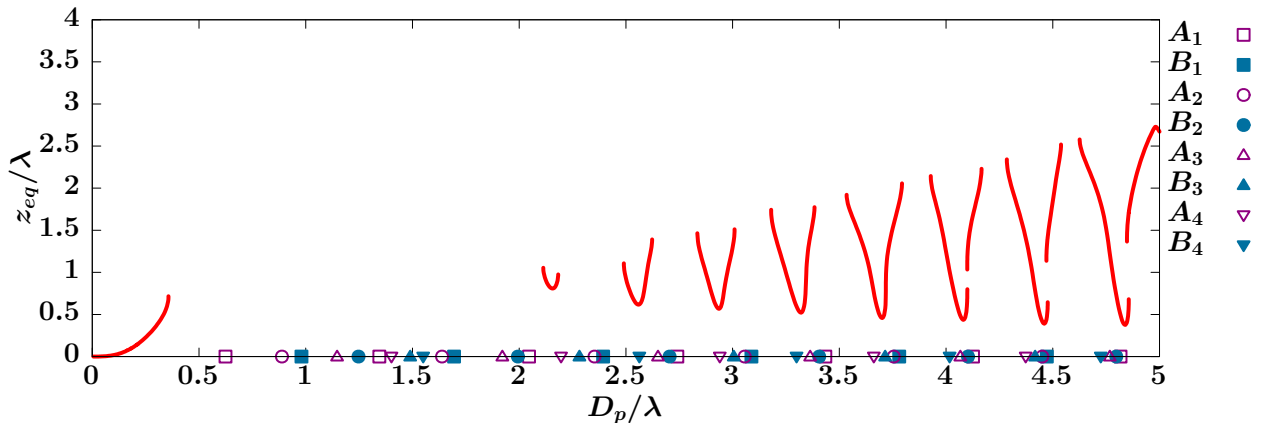


Figure 5: (Color online) On-axis coordinate of axially stable zero-force points z_{eq} as a function of the size parameter for the Gaussian beam.

We consider the case where the thermal noise can be neglected and dynamics of the particle is governed by the equation of motion

$$\frac{d^2\mathbf{r}_p}{dt^2} + 2\gamma\frac{d\mathbf{r}_p}{dt} = m_p^{-1}\mathbf{F}(\mathbf{r}_p), \quad (65)$$

where $\mathbf{F}(\mathbf{r}_p)$ is the optical force given in Eq. (41); γ is the damping constant of the ambient medium and m_p is the mass of the particle.

When the particle is trapped, it is localized in the vicinity of a stable equilibrium (steady state) \mathbf{r}_{eq} , which is the zero-force position where $\mathbf{F}(\mathbf{r}_{\text{eq}}) = \mathbf{0}$. Stability of the equilibrium can be studied in the linear approximation where Eq. (65) is approximated by the first-order (linearized) dynamic equations

$$\frac{d\mathbf{v}}{dt} + 2\gamma\mathbf{v} + \mathbf{L}_0\mathbf{x} = \mathbf{0}, \quad \frac{d\mathbf{x}}{dt} = \mathbf{v}, \quad (66)$$

$$\mathbf{L}_0 \equiv -m_p^{-1}\mathbf{K}_{\text{eq}} \quad (67)$$

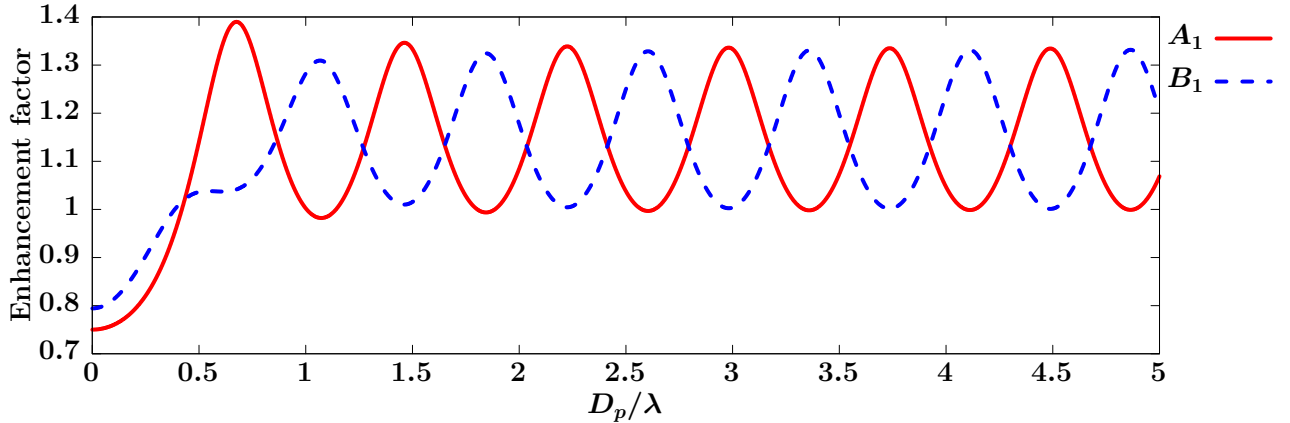


Figure 6: (Color online) Enhancement factors, $A_j = |a_j^{(p)}|^2$ and $B_j = |b_j^{(p)}|^2$, expressed in terms of the internal field coefficients (see Eqs. (10) and (11)) as a function of the size parameter at $j = 1$.

where $\mathbf{x} = \mathbf{r}_p - \mathbf{r}_{\text{eq}}$ is the displacement vector and $\mathbf{K}_{\text{eq}} = \mathbf{K}(\mathbf{r}_{\text{eq}})$ is the stiffness matrix given in Eq. (59).

General solution of the system (66) written in the form

$$\begin{pmatrix} \mathbf{x}(t) \\ \mathbf{v}(t) \end{pmatrix} = \mathbf{U}(t - t_0) \begin{pmatrix} \mathbf{x}(t_0) \\ \mathbf{v}(t_0) \end{pmatrix} \quad (68)$$

describes how the position and the velocity of the particle evolve in time using the evolution operator $\mathbf{U}(t)$ given by

$$\mathbf{U}(t) = e^{-\gamma t} \begin{pmatrix} \cos \sqrt{\mathbf{L}}t & \sqrt{\mathbf{L}^{-1}} \sin \sqrt{\mathbf{L}}t \\ -\sqrt{\mathbf{L}} \sin \sqrt{\mathbf{L}}t & \cos \sqrt{\mathbf{L}}t \end{pmatrix}, \quad \mathbf{L} = \mathbf{L}_0 - \gamma^2 \mathbf{I}_3, \quad (69)$$

where \mathbf{I}_3 is the 3×3 identity matrix.

If the evolution operator (69) contains terms that are unbounded functions of time for $t \in [0, \infty)$, the equilibrium \mathbf{r}_{eq} is unstable [60] and the particle cannot be trapped at such a fixed point. Stability of the equilibrium thus requires the norm of the matrix exponentials $\exp[-\gamma \mathbf{I}_3 \pm i\sqrt{\mathbf{L}}]t$ to be a bounded function of time and is determined by the spectrum of the matrix \mathbf{L} . More specifically, for the zero-force point to be stable, the eigenvalues of the matrix \mathbf{L}_0 must satisfy the inequality

$$|\text{Im}(\sqrt{\Lambda_i - \gamma^2})| \leq \gamma, \quad (70)$$

where Λ_i is the eigenvalue of the matrix \mathbf{L}_0 . After some rather straightforward algebraic manipulations, we can conveniently render the stability condition (71) into the form of the constraint

$$4\gamma^2 \text{Re} \Lambda_i \geq [\text{Im} \Lambda_i]^2 \quad (71)$$

imposed on the value of the damping constant γ .

Inequality (71) suggests that the eigenvalues may generally be divided into the three groups:

- (a) at $\text{Re } \Lambda_i < 0$, the point is unstable and cannot be stabilized by introducing energy losses caused by the ambient medium;
- (b) at $\text{Re } \Lambda_i > 0$ and $\text{Im } \Lambda_i = 0$, the point is stable even if $\gamma = 0$ (the case of vacuum);
- (c) at $\text{Re } \Lambda_i > 0$ and $\text{Im } \Lambda_i \neq 0$, the point is conditionally stable (stabilizable) meaning that, even though the point is unstable at $\gamma = 0$, it can be stabilized provided the particle is embedded into the medium with sufficiently large damping constant γ .

Note that an eigenvalue of \mathbf{L}_0 with $\text{Re } \Lambda_i = 0$ may present different cases depending on its imaginary part. More precisely, the point being conditionally stable at $\text{Im } \Lambda_i = 0$ would be unstable otherwise.

Another remark concerns the non-generic case when the matrix \mathbf{L}_0 is not diagonalizable and its Jordan normal form contains a Jordan block. This may happen only if there are repeated eigenvalues of \mathbf{L}_0 which geometric multiplicity is strictly less than the algebraic one. As opposed to the case of diagonalizable matrix, at the boundary of the stability region where $|\text{Im}(\sqrt{\Lambda_i - \gamma^2})| = \gamma$, the exponentials $\exp[-\gamma \mathbf{I}_3 \pm i\sqrt{\mathbf{L}}]t$ will diverge at $t \rightarrow \infty$ and the zero-force point is unstable.

Now, similar to the force efficiency (53), we introduce the dimensionless effective stiffness matrix

$$\mathbf{L}_{\text{eff}} = \mathbf{L}_0 / L_{\text{scl}}, \quad L_{\text{scl}} = F_{\text{scl}} / (\lambda m_p), \quad (72)$$

where the force scale factor F_{scl} is given in Eq. (53), and present the results of our numerical analysis for the technologically important case of fixed points located on the laser beam axis (the z axis), $\mathbf{r}_{\text{eq}} = (0, 0, z_{\text{eq}})$.

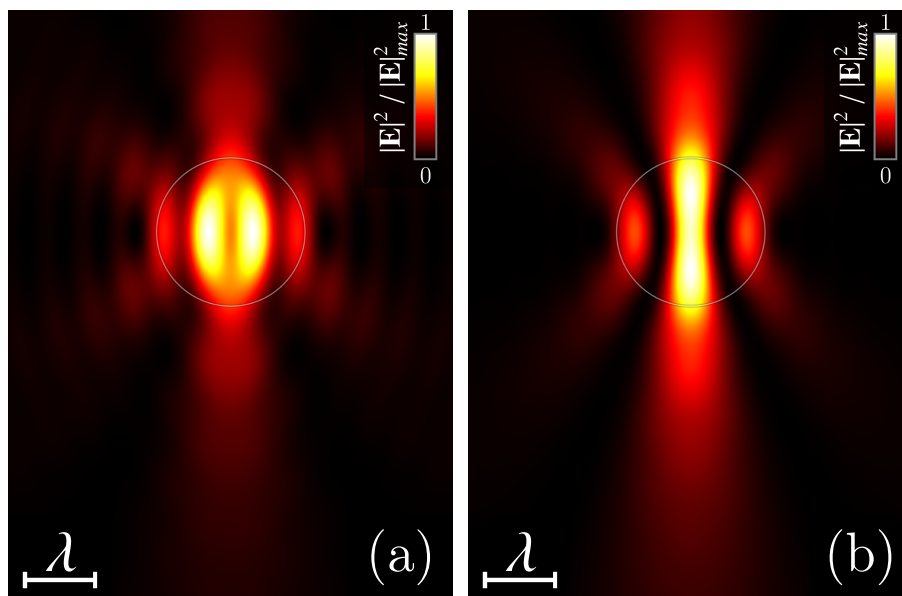


Figure 7: (Color online) Intensity distributions of the incident wave field in (a) the $x - z$ plane and (b) the $y - z$ plane for the non-vertex LG_{10} beam with $f = 0.3$. The z axis is directed from the top down.

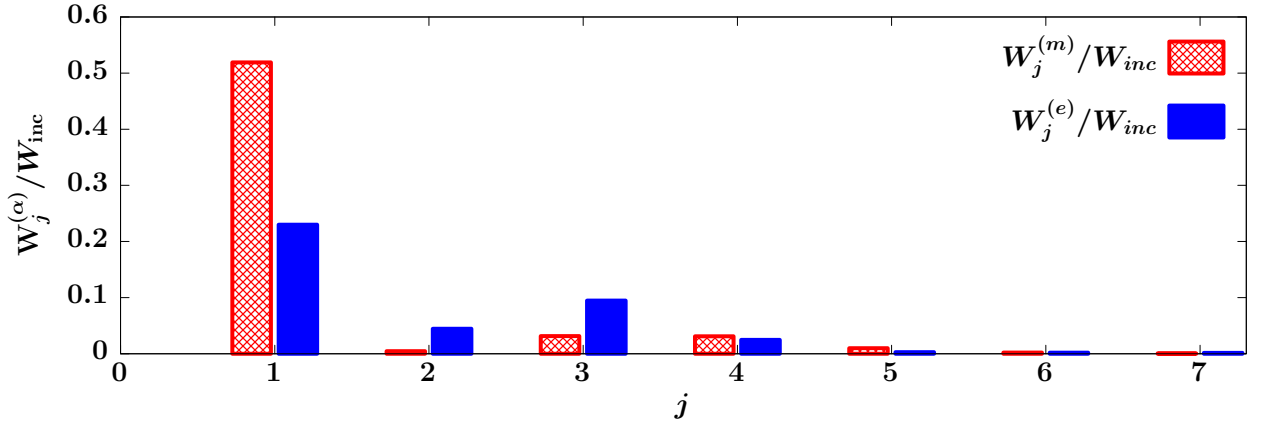


Figure 8: (Color online) Histogram of multipolar decomposition of the incident LG_{10} beam with $f = 0.3$. Height of the bars represents relative contribution of the modes, $W_j^{(m)}/W_{\text{inc}}$ and $W_j^{(e)}/W_{\text{inc}}$, (see Eqs. (36) and (37)) to the total power of the incident beam depending on the angular momentum number j .

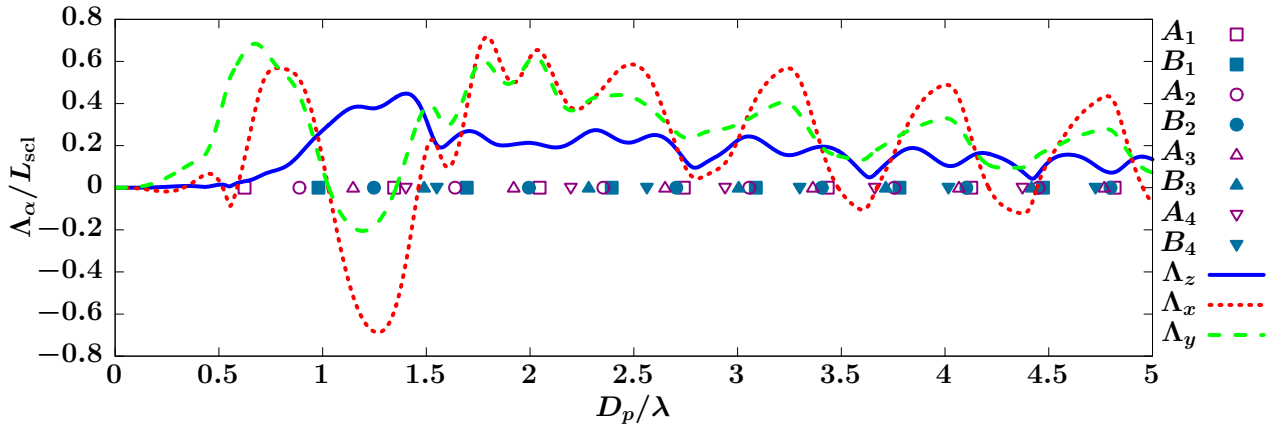


Figure 9: (Color online) Eigenvalues of the effective stiffness matrix \mathbf{L}_{eff} (see Eqs. (72) and (73)), $\Lambda_\alpha/L_{\text{scl}}$, as a function of the size parameter for the LG_{10} beam with $f = 0.3$. The scale factor is $L_{\text{scl}} = nW_{\text{inc}}/(c\lambda m_p)$ (see Eq. (72)).

B. Non-vortex beams with $m_{\text{LG}} = 0$

We begin with the results for non-vortex LG beams characterized by the vanishing azimuthal mode number $m_{\text{LG}} = 0$. The well known example of such beams is the Gaussian beam, LG_{00} , where the radial mode number is also equal to zero. Figure 2 shows the two-dimensional (2D) intensity distributions in the $x-z$ and $y-z$ plane for the LG_{00} beam with the focusing parameter $f = 0.3$. Multipolar decomposition representing the total power of the incident LG_{00} beam resolved into the contributions from the electric and magnetic modes with different angular momentum number j (see Eq. (36)) is presented in Fig. 3.

From our symmetry analysis performed in Sec. IV B, for the non-vortex beams, the stiffness matrix is diagonal (see Eq. (63)). So, the matrix (67) takes the diagonal form:

$$\mathbf{L}_0 = -m_p^{-1} \text{diag}(K_{xx}^{(\text{eq})}, K_{yy}^{(\text{eq})}, K_{zz}^{(\text{eq})}) \equiv \text{diag}(\Lambda_x, \Lambda_y, \Lambda_z), \quad (73)$$

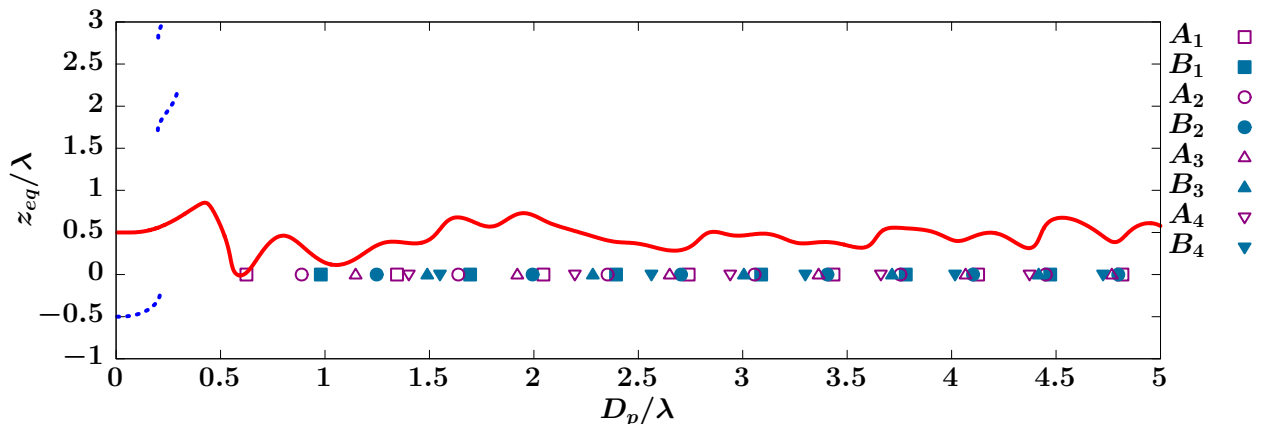


Figure 10: (Color online) On-axis coordinate of axially stable zero-force points z_{eq} as a function of the size parameter for the LG_{10} beam.

where the eigenvalues are equal to the real-valued diagonal elements of \mathbf{L}_0 .

In the linear approximation, these eigenvalues dictate the dynamical regime of the particle motion along the coordinate axes. In particular, the longitudinal mode governed by the eigenvalue

$$\Lambda_z = -m_p^{-1} K_{zz}^{(\text{eq})} \quad (74)$$

determine the axial stability of the zero-force point. In what follows we confine our analysis to the case of the axially stable equilibrium points with $\Lambda_z \geq 0$. The results for these points are shown in Figs. 4 and 5. Referring to Fig. 4, the transverse eigenvalues Λ_x and Λ_y being close to each other are considerably greater than the longitudinal one: $\Lambda_x \approx \Lambda_y > \Lambda_z$. So, it turned out that all the axially stable equilibria are the trapping points (stable zero-force points). The coordinate of the trapping point plotted in relation to the size parameter of the particle, $D_p/\lambda = 2R_p/\lambda$, is depicted in Fig. 5.

In Figs. 4 and 5, differently shaped marks are used to indicate the Mie resonance values of the scatterer size parameter for various modes. Such resonances also known as the morphology-dependent resonances (the whispering gallery modes) reveal themselves in non-monotonic oscillating behavior of the magnitude of the internal field coefficients given by Eqs. (10) and (11). For the enhancement factors defined as the square of the modulus of the internal field coefficients, $A_j = |a_j^{(p)}|^2$ and $B_j = |b_j^{(p)}|^2$, with $j = 1$, such oscillations can be seen in Fig. 6. Open and filled squares are used to mark the values of the size parameter D_p/λ corresponding to local maxima of the enhancement factors A_1 and B_1 , respectively.

The LG_{10} beam characterized by the intensity distributions and the multipolar decomposition shown in Figs. 7 and 8, respectively, presents the case of a non-vertex incident beam with nonzero radial mode number. By contrast to the case of the Gaussian beams, as is seen from Fig. 9, the longitudinal eigenvalue, Λ_z , and the transverse stiffness coefficients, Λ_x and Λ_y , are of the same order.

Referring to Fig. 9, for the LG_{10} beam, stability of equilibria is determined by the sign of the transverse eigenvalue Λ_x , whereas, for the Gaussian beam, the stability governing factor is the sign of Λ_z . In addition, the size parameter dependence of the zero-force point coordinate shown in Fig. 10 demonstrates the presence of several branches of axially stable equilibria in the region of subwavelength scatterers.

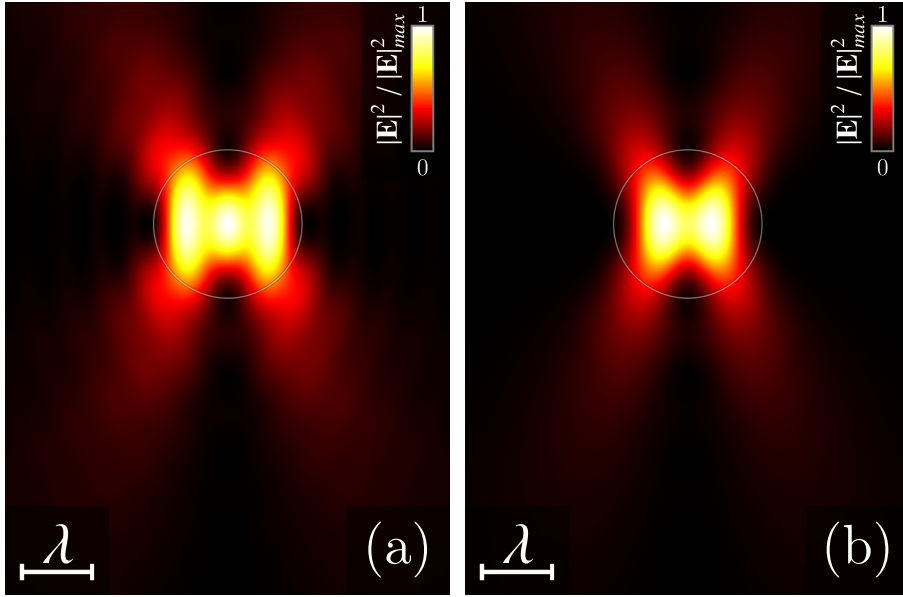


Figure 11: (Color online) Intensity distributions of the incident wave field in (a) the $x - z$ plane and (b) the $y - z$ plane for the LG_{01} beam with $f = 0.3$. The z axis is directed from the top down.

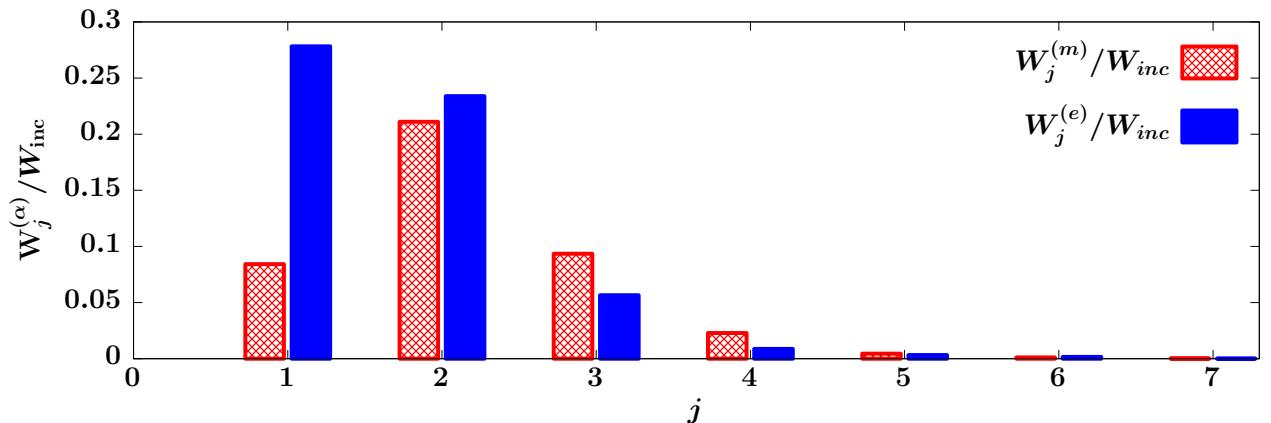


Figure 12: (Color online) Histogram of multipolar decomposition of the incident LG_{01} beam with $f = 0.3$. Height of the bars represents relative contribution of the modes, $W_j^{(m)}/W_{inc}$ and $W_j^{(e)}/W_{inc}$, (see Eqs. (36) and (37)) to the total power of the incident beam depending on the angular momentum number j .

C. Optical vortex beams: effects of non-conservative dynamics

It should be stressed that, for the above discussed case of non-vortex beams is characterized by the symmetric stiffness matrix and the dynamics of the particle is thus locally conservative.

Since all the eigenvalues of such matrices are real, there are no conditionally stable equilibria and stability of all the zero-force points turned out to be essentially independent of the ambient damping. For the laser beams carrying a phase singularity known as the vortex the latter is no longer the case.

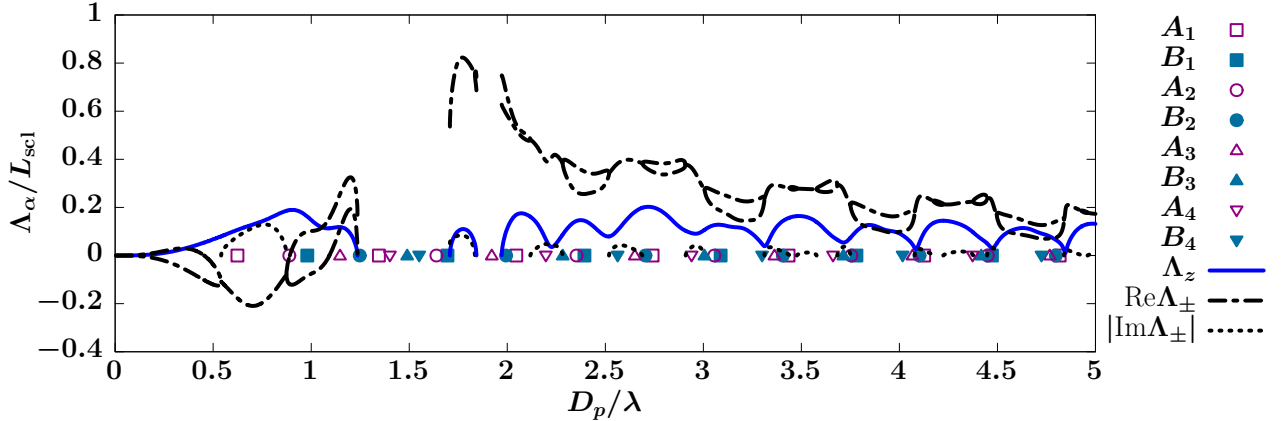


Figure 13: (Color online) Eigenvalues of the effective stiffness matrix \mathbf{L}_{eff} (see Eqs. (72) and (75)), $\Lambda_\alpha/L_{\text{scl}}$, as a function of the size parameter for the LG₀₁ beam with $f = 0.3$.

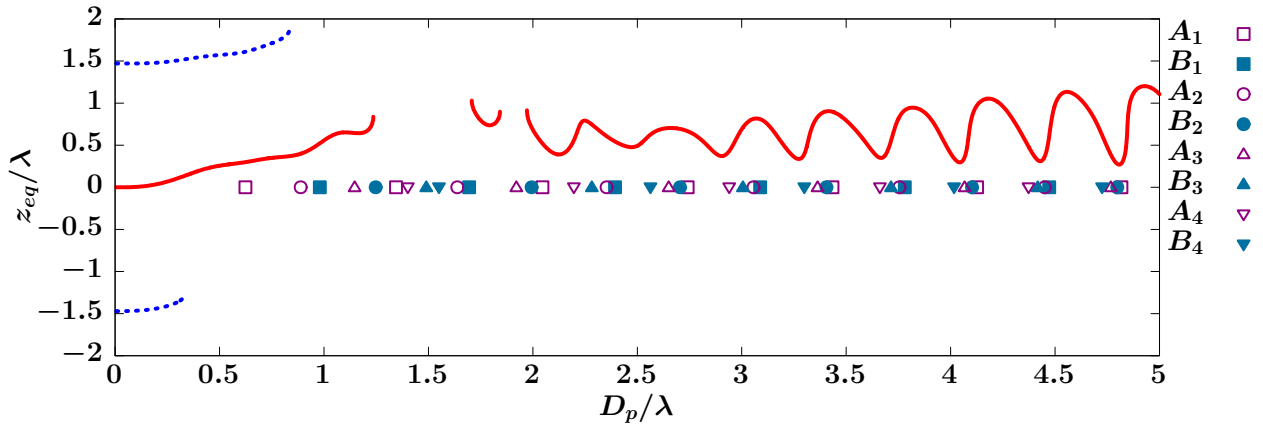


Figure 14: (Color online) On-axis coordinate of axially stable zero-force points z_{eq} as a function of the size parameter for the LG₀₁ beam.

The topological charge characterizing the phase singularity and associated orbital angular momentum are known to produce a rich variety of phenomena [40] such as rotation of trapped spheres by vortex beams [41, 42]. The latter is a remarkable manifestation of the non-conservative nature of optical-force-induced dynamics meaning that optical forces cannot generally be derived from an underlying potential. The optical force field includes a scattering contribution, and asymmetric couplings will occur between coordinates which will lead to asymmetric stiffness matrices [44, 61].

In this section, we consider purely azimuthal LG beams [62] with $n_{\text{LG}} = 0$ and $m_{\text{LG}} \neq 0$ that represent optical vortex beams. Symmetry of such beams has been discussed in Sec. IV B leading to the conclusion that the linearized dynamics is governed by the non-

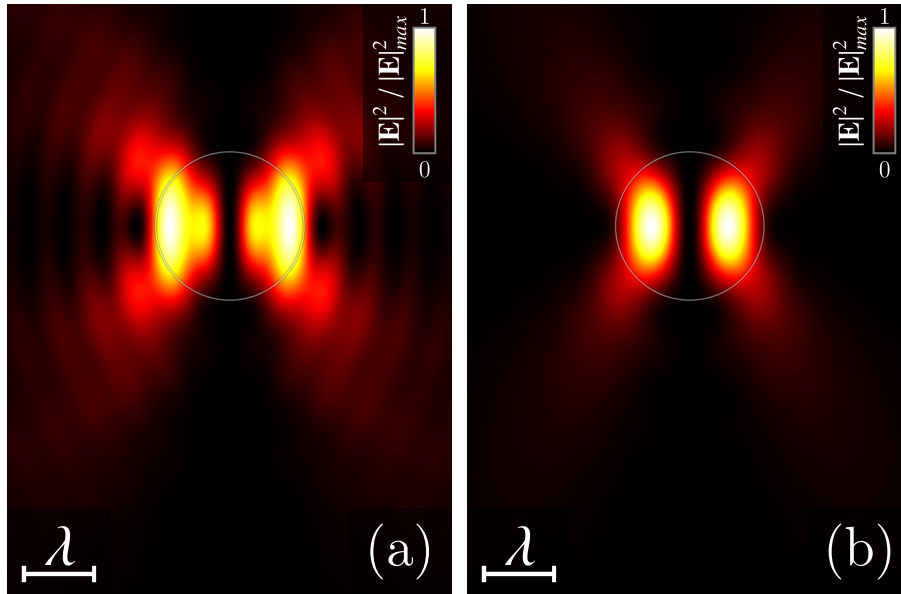


Figure 15: (Color online) Intensity distributions of the incident wave field in (a) the $x - z$ plane and (b) the $y - z$ plane for the LG_{02} beam with $f = 0.3$. The z axis is directed from the top down.

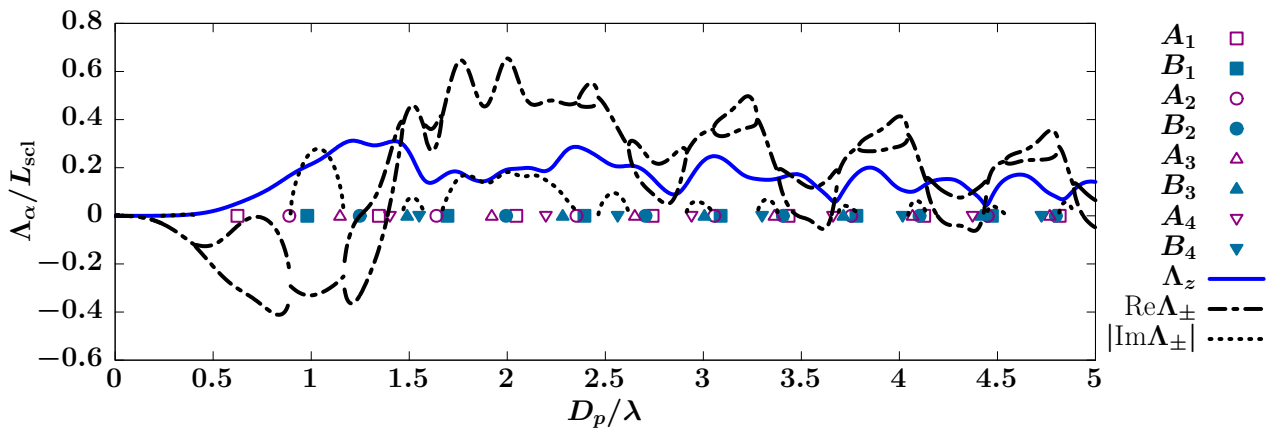


Figure 16: (Color online) Eigenvalues of the effective stiffness matrix \mathbf{L}_{eff} (see Eqs. (72) and (75)), $\Lambda_\alpha / L_{\text{scl}}$, as a function of the size parameter for the LG_{02} beam with $f = 0.3$.

symmetric stiffness matrix of the form:

$$\mathbf{L}_0 = -m_p^{-1} \begin{pmatrix} K_{xx}^{(\text{eq})} & K_{xy}^{(\text{eq})} & 0 \\ K_{yx}^{(\text{eq})} & K_{yy}^{(\text{eq})} & 0 \\ 0 & 0 & K_{zz}^{(\text{eq})} \end{pmatrix} = \text{diag}(\mathbf{L}_t, \Lambda_z), \quad (75)$$

$$\mathbf{L}_t = \begin{pmatrix} L_{11} & L_{12} \\ L_{21} & L_{22} \end{pmatrix} = -m_p^{-1} \begin{pmatrix} K_{xx}^{(\text{eq})} & K_{xy}^{(\text{eq})} \\ K_{yx}^{(\text{eq})} & K_{yy}^{(\text{eq})} \end{pmatrix}. \quad (76)$$

Formula (75) shows that, similar to the case of non-vortex beams, the eigenvalue Λ_z given by Eq. (74) controls axial stability of the equilibria whereas the eigenvalues of the matrix (76)

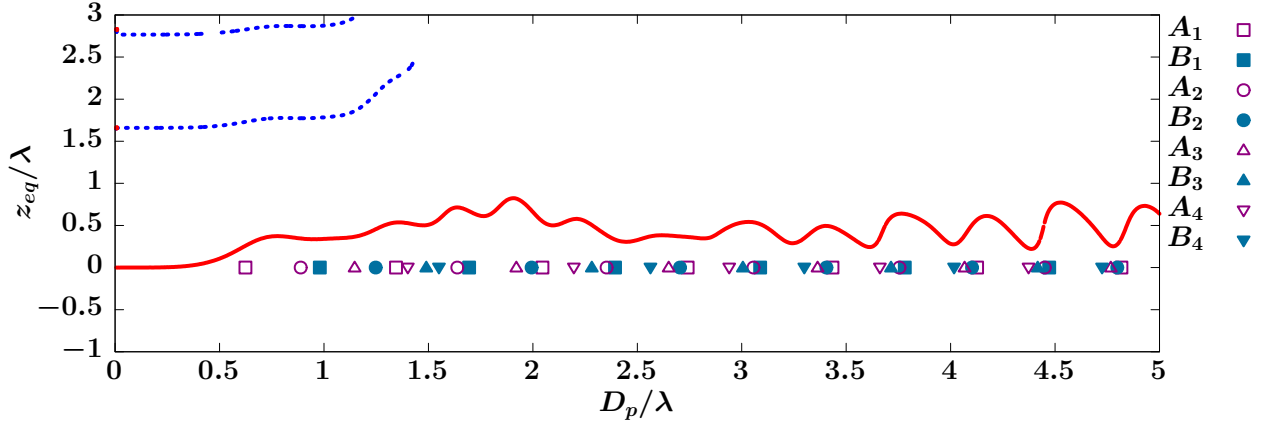


Figure 17: (Color online) On-axis coordinate of axially stable zero-force points z_{eq} as a function of the size parameter for the LG_{02} beam.

(the transverse eigenvalues)

$$\Lambda_{\pm} = L_{\pm} \pm \sqrt{L_{-}^2 + L_{12}L_{21}}, \quad L_{\pm} = (L_{11} \pm L_{22})/2 \quad (77)$$

dictate the dynamics in the transverse plane (the $x - y$ plane) and govern the radial (transverse) stability of the zero-force points.

Figures 11 and 12 present the intensity distributions and the mode decomposition for the focused LG_{01} beam remodelled using the focusing parameter $f = 0.3$. The eigenvalues and the coordinate of the axially stable zero-force point computed as a function of the size parameters are shown in Figs. 13 and 14, respectively.

From the plots depicted in Fig. 13, the zero-force point is axially unstable in the two intervals which upper boundary points appear to be close to the size ratio D_p/λ corresponding the local maxima (the Mie resonances) of the enhancement factors B_2 ($D_p/\lambda \approx 1.25$ and $D_p/\lambda \approx 2.0$) and B_1 ($D_p/\lambda \approx 1.65$). In the remaining part of the size parameter region, stability is determined by the transverse eigenvalues (77).

Referring to Fig. 13, the interval separating the regions of axial instability, represent the conditionally unstable points with $\text{Re } \Lambda_{+} = \text{Re } \Lambda_{-} > 0$ and $\text{Im } \Lambda_{\pm} \neq 0$. By contrast, in the region of small particles, the equilibrium points are mainly unstable except for the small interval of stable points ($\text{Re } \Lambda_{+} > \text{Re } \Lambda_{-} > 0$ and $\text{Im } \Lambda_{\pm} = 0$) located below the Mie resonance point at $D_p/\lambda \approx 1.25$.

For larger particles, at $D_p/\lambda > 1.65$, the Λ_{\pm} curves indicate the presence of both stable and conditionally stable trapping points. This is the region where, as it can be seen from Fig. 14, the size dependence of the equilibrium coordinate z_{eq} shows increasingly oscillating behavior with minima located near certain Mie resonance values of the size parameter.

Note that, in the 2D distributions for the beams with $m_{LG} = 1$ shown in Fig. 11, the intensity is clearly nonzero on the z axis in the near-field region localized inside the scatterer. According to Ref. [36], the near-field contributions to the electric field that are linearly polarized along the propagation axis are responsible for destroying the vortex.

As is evident from the intensity distributions presented in Fig. 15, there are no such effects for the LG_{02} beams with $m_{LG} = 2$. For such beams, the results for the eigenvalues of the stiffness matrix plotted in Fig. 16 indicate that, similar to the LG_{10} beams (see Fig. 9), all the zero-force points are axially stable. It can also be seen that the endpoints of the

instability and conditional stability intervals correlate well with the Mie resonances. As in the case of the LG_{01} beams, in the large particle region with $D_p/\lambda > 3$, the size dependence of the equilibrium coordinate shown in Fig. 17 reveals the oscillating regime with minima related to the resonances. Another effect shared by all the non-Gaussian beams under consideration is the presence of additional branches of axially stable equilibria provided the size of the particle is sufficiently small (see Figs. 10, 14 and 17). These branches, however, predominantly represent radially unstable equilibria and we have omitted the corresponding results for the eigenvalues.

VI. CONCLUSIONS

In this paper, we have studied the optical-force-induced dynamics of Mie particles illuminated with LG beams. For this purpose, we have used a T -matrix approach in the form described in Refs. [14, 36]. Our approach also uses the remodeling procedure in which the far-field matching method is combined with the results for nonparaxial propagation of LG beams. Scattering of such beams is thus described in terms of the far-field angular distributions, $\mathbf{E}_{\text{out}}^{(\text{inc})}$ and $\mathbf{E}_{\text{out}}^{(\text{sca})}$, that determine the outgoing parts of the incident and scattered waves [see Eqs. (25) and (26)]. The far-field distributions play the central part in the method giving, in particular, the differential cross-sections [see Eqs. (34) and (35)] and the optical (radiation) force acting upon the Mie scatterer [see Eq. (41)].

The symmetry analysis performed in Sec. IV for the LG beams with the far-field distribution given by Eq. (31a) have shown that, owing to the twofold rotational symmetry [see Eq. (60)], the stiffness matrix (59) is generally non-symmetric and non-diagonal [see Eq. (61)] provided the LG beam carries the optical vortex with the topological charge characterized by the azimuthal number m_{LG} . By contrast, for the non-vortex LG beams with $m_{\text{LG}} = 0$, the stiffness matrix is diagonal (see Eq. (63)). The form of the beam shape coefficients (64) is also dictated by the twofold rotational symmetry of the LG beam.

The analytical results for the optical force and the stiffness matrix are employed to perform numerical analysis of the dynamics of the particle embedded into the viscous medium characterized by the damping constant γ [the equation of motion is given by Eq. (65)]. In this analysis, we have examined stability of the zero-force axial points and the associated regimes of the linearized dynamics governed by Eq. (66). These regimes are shown to be dictated by the eigenvalues of the stiffness matrix (67) that enter the stability condition (70). From this condition, the steady state points are found to fall into the three following categories: (a) the unstable points with $\text{Re } \Lambda_i < 0$; (b) the stable points with $\text{Re } \Lambda_i = \Lambda_i > 0$ (these are the trapping points that remain stable even if $\gamma = 0$); and (c) the conditionally stable (stabilizable) points with $\text{Re } \Lambda_i \neq \Lambda_i > 0$ (such points being unstable at $\gamma = 0$ can be stabilized provided the damping constant is sufficiently large).

Figures 2–10 present the results for incident non-vortex LG beams with vanishing azimuthal number, $m_{\text{LG}} = 0$, and the focusing parameter $f = 0.3$ ($2\pi f = \lambda/w_0$). The Gaussian (LG_{00}) and non-Gaussian (LG_{10}) beams (the intensity distributions are shown in Figs. 2 and 7, respectively) are both characterized by the diagonal stiffness matrix (73) and stability of the equilibria is thus independent of the ambient medium. The longitudinal eigenvalue Λ_z given by Eq. (74) controls the axial stability of the equilibrium points and all our results for the eigenvalues and the location of equilibria are limited to the case of axially stable points with $\Lambda_z > 0$.

Referring to Figs. 4 and 5, this is the axial stability that determines stability of the

trapping points depending on the size parameter D_p/λ of the particle illuminated with the Gaussian beam. By contrast, the results for the non-Gaussian LG₁₀ beam shown in Figs. 9 and 10 indicate that all the points are axially stable and their stability is governed by the size dependence of the transverse eigenvalue Λ_x .

The principal characteristic feature of the conservative radiation-force-induced dynamics illustrated by the non-vortex LG beams is that the stiffness matrix is symmetric and its eigenvalues are real-valued. Therefore, such dynamics is characterized by the absence of conditionally stable points with $\text{Im } \Lambda_i \neq 0$.

We have found that, for purely azimuthal LG beams with the vanishing radial number, $n_{\text{LG}} = 0$, and the nonzero azimuthal mode number $m_{\text{LG}} \in \{1, 2\}$, the latter is no longer the case. Such beams (the intensity distributions for the LG₀₁ and LG₀₂ beams are shown in Figs. 11 and 15, respectively) represent the case of optical vortex LG beams carrying a phase singularity and exhibiting a helical phase front.

Equation (77) gives the transverse eigenvalues of the stiffness matrix (75) for the optical vortex beams. The eigenvalues computed as a function of the size parameter for the LG₀₁ and LG₀₂ beams are plotted in Figs. 13 and 16, respectively. These figures clearly indicate the intervals of the size parameter where the equilibrium points are conditionally stable with $\text{Im } \Lambda_{\pm} \neq 0$ and $\text{Re } \Lambda_+ = \text{Re } \Lambda_- > 0$. In both cases, at small values of the size parameter, the transverse eigenvalues play the role of the destabilizing factor. For the LG₀₁ beam, similar to the Gaussian beam, stability of the equilibria outside the region of small scatterers is controlled by the longitudinal eigenvalue Λ_z . When $m_{\text{LG}} = 2$, the zero-force points are axially stable and, similar to the case of the LG₁₀ beam, stability is determined by the transverse eigenvalues, Λ_+ and Λ_- .

In figures showing the curves for the eigenvalues and the equilibrium coordinate z_{eq} , we have used differently shaped symbols to mark the values of the size parameter D_p/λ corresponding to local maxima of the enhancement factors $A_j = |a_j^{(p)}|^2$ and $B_j = |b_j^{(p)}|^2$, where $a_j^{(p)}$ and $b_j^{(p)}$ are the internal field coefficients. For non-Gaussian LG beams, the endpoints of the instability and conditional stability intervals are found to be close to certain Mie resonance points. Similar remark applies to the minima characterizing oscillating behavior of the size dependence of z_{eq} in the large size region. The resonances in the Mie coefficients and the related interference effects are thus found to play the role of the factor changing the trapping properties of the particles. Similarly, the results of Ref. [63] show that the Mie resonances have a profound effect on the trapping characteristics of high refractive index particles where the interference effects are expected to be strongest.

In conclusion, we note that our symmetry considerations tacitly assume that the incident beam is solely responsible for breaking the spherical symmetry of the optically isotropic dielectric scatterer. The symmetry can additionally be reduced by the optical anisotropy [14, 54] that may thus significantly affect the regimes of the radiation-force-induced dynamics of the particle. Despite some recent results on the radiation force exerted on uniaxially anisotropic spheres [64, 65], the optical anisotropy related effects are still far from being well understood.

ACKNOWLEDGMENTS

ADK acknowledges partial financial support from the Government of the Russian Federation (Grant No. 074-U01), from the Ministry of Education and Science of the Russian Fed-

eration (Grant No. GOSZADANIE 2014/190, Project No. 14.Z50.31.0031, and ZADANIE Grant No. 1.754.2014/K), through a grant from the Russian Foundation for Basic Research, and through a grant from the President of Russia (Grant No. MK-2736.2015.2).

-
- [1] A. Ashkin, “Acceleration and trapping of particles by radiation pressure,” *Phys. Rev. Lett.* **24**, 156–159 (1970).
 - [2] Arthur Ashkin, *Optical Trapping and Manipulation of Neutral Particles Using Lasers: A Reprint Volume with Commentaries* (World Scientific, London, 2006) p. 466.
 - [3] A. Ashkin, J. M. Dziedzic, J. E. Bjorkholm, and Steven Chu, “Observation of a single-beam gradient force optical trap for dielectric particles,” *Opt. Lett.* **11**, 288–290 (1986).
 - [4] Timo A. Nieminen, Nathaniel du Preez-Wilkinson, Alexander B. Stilgoe, Vincent L.Y. Loke, Ann A.M. Bui, and Halina Rubinsztein-Dunlop, “Optical tweezers: Theory and modelling,” *J. of Quant. Spectr. & Radiat. Transf.* **146**, 59–80 (2014).
 - [5] Alessandro Salandrino, Shima Fardad, and Demetrios N. Christodoulides, “Generalized Mie theory of optical forces,” *J. Opt. Soc. Am. B* **29**, 855–866 (2012).
 - [6] G. Mie, “Beiträge zur Optik trüber Medien, speziell kolloidaler Metallösungen,” *Ann. Phys. (Leipzig)* **25**, 377–445 (1908).
 - [7] R. G. Newton, *Scattering Theory of Waves and Particles*, 2nd ed. (Springer, Heidelberg, 1982) p. 745.
 - [8] Leung Tsang, Jin Au Kong, and Kung-Hau Ding, *Scattering of Electromagnetic Waves. Theories and Applications*, Wiley Series in Remote Sensing, Vol. 1 (Wiley-Interscience Pub, NY, 2000) p. 426.
 - [9] Michael I. Mishchenko, Larry D. Travis, and Andrew A. Lacis, *Scattering, Absorption and Emission of Light by Small Particles* (Cambridge University Press, NY, 2004) p. 448.
 - [10] Gérard Gouesbet and Gérard Gréhan, *Generalized Lorenz–Mie theories* (Springer, Berlin, 2011) p. 310.
 - [11] M. I. Mishchenko, L. D. Travis, and D. W. Mackowski, “*T*-matrix computations of light scattering by nonspherical particles: a review,” *J. of Quant. Spectr. & Radiat. Transf.* **55**, 535–575 (1996).
 - [12] M. I. Mishchenko, J. W. Hovenier, and L. D. Travis, eds., *Light Scattering by Nonspherical Particles: Theory, Measurements and Applications* (Academic Press, New York, 2000).
 - [13] A. D. Kiselev, V. Yu. Reshetnyak, and T. J. Sluckin, “Influence of the optical axis distribution in the anisotropic layer surrounding a spherical particle on the scattering of light,” *Opt. Spectrosc.* **89**, 907–913 (2000).
 - [14] A. D. Kiselev, V. Yu. Reshetnyak, and T. J. Sluckin, “Light scattering by optically anisotropic scatterers: T-matrix theory for radial and uniform anisotropies,” *Phys. Rev. E* **65**, 056609 (2002).
 - [15] Y.-L. Geng, X.-B. Wu, L.-W. Li, and B.-R. Guan, “Mie scattering by a uniaxial anisotropic sphere,” *Phys. Rev. E* **70**, 056609 (2004).
 - [16] Andrey Novitsky and Leonid Barkovsky, “Matrix approach for light scattering from a multi-layered rotationally symmetric bianisotropic sphere,” *Phys. Rev. A* **77**, 033849 (2008).
 - [17] Chengwei Qiu, Lei Gao, John D. Joannopoulos, and Marin Soljačić, “Light scattering from anisotropic particles: propagation, localization and nonlinearity,” *Laser & Photon. Rev.* **4**, 268–282 (2010).

- [18] Gerard Grehan, B. Maheu, and Gerard Gouesbet, “Scattering of laser beams by Mie scatter centers: numerical results using a localized approximation,” *Appl. Opt.* **25**, 3539–3548 (1986).
- [19] G. Gouesbet, B. Maheu, and G. Gréhan, “Light scattering from a sphere arbitrarily located in a Gaussian beam, using a Bromwich formulation,” *J. Opt. Soc. Am. A* **5**, 1427–1443 (1988).
- [20] J. P. Barton, D. R. Alexander, and S. A. Schaub, “Internal and near-surface electromagnetic fields for a spherical particle irradiated by a focused laser beam,” *J. Appl. Phys.* **64**, 1632–1639 (1988).
- [21] J. P. Barton, D. R. Alexander, and S. A. Schaub, “Theoretical determination of net radiation force and torque for a spherical particle illuminated by a focused laser beam,” *J. Appl. Phys.* **66**, 4594–4602 (1989).
- [22] S. A. Schaub, D. R. Alexander, and J. P. Barton, “Glare spot image calculations for a spherical particle illuminated by a tightly focused beam,” *J. Opt. Soc. Am. A* **9**, 316–330 (1992).
- [23] James A. Lock and Gérard Gouesbet, “Generalized Lorenz-Mie theory and applications,” *J. of Quant. Spectr. & Radiat. Transf.* **110**, 800–807 (2009).
- [24] G. Gouesbet, J. A. Lock, and G. Gréhan, “Generalized Lorenz–Mie theories and description of electromagnetic arbitrary shaped beams: Localized approximations and localized beam models, a review,” *J. of Quant. Spectr. & Radiat. Transf.* **112**, 1–27 (2011).
- [25] M. Lax, W. H. Louisell, and W. B. McKnight, “From Maxwell to paraxial wave optics,” *Phys. Rev. A* **11**, 1365–1370 (1975).
- [26] T. A. Nieminen, H. Rubinsztein-Dunlop, and N. R. Heckenberg, “Multipole expansion of strongly focussed laser beams,” *J. of Quant. Spectr. & Radiat. Transf.* **79–80**, 1005–1017 (2003).
- [27] Paul B. Bareil and Yunlong Sheng, “Modeling highly focused laser beam in optical tweezers with the vector Gaussian beam in the T-matrix method,” *J. Opt. Soc. Am. A* **30**, 1–6 (2013).
- [28] Thanh Xuan Hoang, Xudong Chen, and Colin J. R. Sheppard, “Multipole theory for tight focusing of polarized light, including radially polarized and other special cases,” *J. Opt. Soc. Am. A* **29**, 32–43 (2012).
- [29] S. M. Barnett and L. Allen, “Orbital angular momentum and nonparaxial light beams,” *Opt. Commun.* **110**, 670–678 (1994).
- [30] K. Duan, B. Wang, and B. Lü, “Propagation of Hermite-Gaussian and Laguerre-Gaussian beams beyond the paraxial approximation,” *J. Opt. Soc. Am. A* **22**, 1976–1980 (2005).
- [31] A. S. Van De Nes, S. F. Pereira, and J. J. M. Braat, “On the conservation of fundamental optical quantities in non-paraxial imaging systems,” *Journal of Modern Optics* **53**, 677–687 (2006).
- [32] Guoquan Zhou, “Analytical vectorial structure of Laguerre–Gaussian beam in the far field,” *Opt. Lett.* **31**, 2616 (2006).
- [33] Guoquan Zhou, “Propagation of a vectorial Laguerre-Gaussian beam beyond the paraxial approximation,” *Optics & Laser Technology* **40**, 930–935 (2008).
- [34] A. S. van de Nes and P. Török, “Rigorous analysis of spheres in Gauss-Laguerre beams,” *Opt. Express* **15**, 13360–13374 (2007).
- [35] Yuesong Jiang, Yuwei Shao, Xiaosheng Qu, Jun Ou, and Houqiang Hua, “Scattering of a focused Laguerre–Gaussian beam by a spheroidal particle,” *J. Opt.* **14**, 125709 (2012).
- [36] Alexei D. Kiselev and Dmytro O. Plutenko, “Mie scattering of Laguerre-Gaussian beams: Photonic nanojets and near-field optical vortices,” *Phys. Rev. A* **89**, 043803 (2014).
- [37] Huachao Yu and Weilong She, “Radiation force exerted on a sphere by focused Laguerre-Gaussian beams,” *J. Opt. Soc. Am. A* **32**, 130–142 (2015).

- [38] T. Otsu, T. Ando, Y. Takiguchi, Y. Ohtake, H. Toyoda, and H. Itoh, “Direct evidence for three-dimensional off-axis trapping with single Laguerre-Gaussian beam,” *Sci. Rep.* **4**, 4579 (2014).
- [39] L. Allen, S. M. Barnett, and M. J. Padgett, eds., *Optical Angular Momentum* (Taylor & Francis, London, 2003).
- [40] David L. Andrews, ed., *Structured Light and Its Applications: An Introduction to Phase-Structured Beams and Nanoscale Optical Forces* (Academic Press, Amsterdam, 2008) p. 342.
- [41] David G. Grier, “A revolution in optical manipulation,” *Nature* **424**, 810–816 (2003).
- [42] Stephen H. Simpson and Simon Hanna, “Rotation of absorbing spheres in Laguerre–Gaussian beams,” *J. Opt. Soc. Am. A* **26**, 173–183 (2009).
- [43] Yohai Roichman, Bo Sun, Allan Stolarski, and David G. Grier, “Influence of Nonconservative Optical Forces on the Dynamics of Optically Trapped Colloidal Spheres: The Fountain of Probability,” *Phys. Rev. Lett.* **101**, 128301 (2008).
- [44] Stephen H. Simpson and Simon Hanna, “First-order nonconservative motion of optically trapped nonspherical particles,” *Phys. Rev. E* **82**, 031141 (2010).
- [45] David B. Ruffner and David G. Grier, “Optical Forces and Torques in Nonuniform Beams of Light,” *Phys. Rev. Lett.* **108**, 173602 (2012).
- [46] Martin Šiler, Petr Jákł, Oto Brzobohatý, and Pavel Zemánek, “Optical forces induced behavior of a particle in a non-diffracting vortex beam,” *Opt. Express* **20**, 24304–24319 (2012).
- [47] Udo Seifert, “Stochastic thermodynamics, fluctuation theorems and molecular machines,” *Rep. Prog. Phys.* **75**, 126001 (2012).
- [48] Bohdan I. Lev and Alexei D. Kiselev, “Energy representation for nonequilibrium brownian-like systems: Steady states and fluctuation relations,” *Phys. Rev. E* **82**, 031101 (2010).
- [49] L. C. Biedenharn and J. D. Louck, *Angular Momentum in Quantum Physics: Theory and Application*, Encyclopedia of Mathematics and its Applications, Vol. 8 (Addison–Wesley, Reading, Massachusetts, 1981) p. 717.
- [50] D. A. Varshalovich, A. N. Moskalev, and V. K. Khersonskii, *Quantum theory of angular momentum: Irreducible tensors, spherical harmonics, vector coupling coefficients, 3nj symbols* (World Scientific Publishing Co., Singapore, 1988) p. 514.
- [51] J. D. Jackson, *Classical Electrodynamics*, 3rd ed. (Wiley, New York, 1999).
- [52] Dipankar Sarkar and N. J. Halas, “General vector basis function solution of Maxwells equations,” *Phys. Rev. E* **56**, 1102–1112 (1997).
- [53] M. Abramowitz and I. A. Stegun, eds., *Handbook of Mathematical Functions* (Dover, New York, 1972).
- [54] A. D. Kiselev, V. Yu. Reshetnyak, and T. J. Sluckin, “T-matrix theory of light scattering by uniformly anisotropic scatterers,” *Mol. Cryst. Liq. Cryst.* **375**, 373–386 (2002).
- [55] B. Stout, M. Nevière, and E. Popov, “Mie scattering by an anisotropic object. Part I. Homogeneous sphere,” *J. Opt. Soc. Am. A* **23**, 1111–1123 (2006).
- [56] J. Roth and M. J. Digman, “Scattering and extinction cross sections for a spherical particle coated with an oriented molecular layer,” *J. Opt. Soc. Am.* **63**, 308–311 (1973).
- [57] I. S. Gradshteyn and I. M. Ryzhik, *Table of Integrals, Series, and Products* (Academic, New York, 1980).
- [58] George C. Sherman, Jakob J. Stamnes, and Éamon Lalor, “Asymptotic approximations to angular–spectrum representations,” *J. Math. Phys.* **17**, 760–776 (1976).
- [59] Michael I. Mishchenko, “Radiation force caused by scattering, absorption and emission of light by nonspherical particles,” *J. of Quant. Spectr. & Radiat. Transf.* **70**, 811–816 (2001).

- [60] John Guckenheimer and Philip Holmes, *Nonlinear oscillations, dynamical systems, and bifurcations of vector fields*, Applied Mathematical Sciences, Vol. 42 (Springer-Verlag, NY, 1990) p. 459.
- [61] Jack Ng, Zhifang Lin, and C. T. Chan, “Theory of Optical Trapping by an Optical Vortex Beam,” *Phys. Rev. Lett.* **104**, 103601 (2010).
- [62] Aaron S. Rury and Richard Freeling, “Mie scattering of purely azimuthal Laguerre-Gauss beams: Angular-momentum-induced transparency,” *Phys. Rev. A* **86**, 053830 (2012).
- [63] Alexander B. Stilgoe, Timo A. Nieminen, Gregor Knöner, Norman R. Heckenberg, and Halina Rubinsztein-Dunlop, “The effect of Mie resonances on trapping in optical tweezers,” *Opt. Express* **16**, 15039–15051 (2008).
- [64] Zheng-Jun Li, Zhen-Sen Wu, Qing-Chao Shang, Lu Bai, and Chun-Hui Cao, “Calculation of radiation force and torque exerted on a uniaxial anisotropic sphere by an incident Gaussian beam with arbitrary propagation and polarization directions,” *Opt. Express* **20**, 16421–16435 (2012).
- [65] Tan Qu, Zhen-Sen Wu, Qing-Chao Shang, Zheng-Jun Li, Lu Bai, and Lei Gong, “Analysis of the radiation force of a Laguerre Gaussian vortex beam exerted on an uniaxial anisotropic sphere,” *J. of Quant. Spectr. & Radiat. Transf.* **162**, 103–113 (2015).

Appendix A: Gradient terms in far-field expression for optical force

In this Appendix we consider the case of non-absorbing scatterer and show how to rearrange the far-field expression for the optical force (41) so as to separate out the gradient part of the force. For this purpose, we begin with the far-field distribution of the scattered wave (26) rewritten in the following form:

$$\begin{aligned} \mathbf{E}_{\text{out}}^{(\text{sca})}(\hat{\mathbf{r}}, \mathbf{r}_p) &\equiv \mathbf{E}_{\text{out}}^{(\text{sca})} = \sum_{jm} \sum_{\alpha \in \{e,m\}} s_{jm}^{(\alpha)}(\mathbf{r}_p) \mathbf{Y}_{jm}^{(\alpha)}(\hat{\mathbf{r}}) = 2 \sum_{jm} \sum_{\alpha \in \{e,m\}} T_j^{(\alpha)} w_{jm}^{(\alpha)}(\mathbf{r}_p) \mathbf{Y}_{jm}^{(\alpha)}(\hat{\mathbf{r}}) \\ &= 2 \langle \mathcal{T}(\hat{\mathbf{r}}, \hat{\mathbf{r}}') \mathbf{E}_{\text{out}}^{(\text{inc})}(\hat{\mathbf{r}}', \mathbf{r}_p) \rangle_{\hat{\mathbf{r}}} \equiv 2 \mathcal{T} \mathbf{E}_{\text{out}}^{(\text{inc})}, \end{aligned} \quad (\text{A1})$$

$$\mathcal{T}(\hat{\mathbf{r}}, \hat{\mathbf{r}}') = \sum_{jm} \sum_{\alpha \in \{e,m\}} T_j^{(\alpha)} \mathbf{Y}_{jm}^{(\alpha)}(\hat{\mathbf{r}}) \otimes [\mathbf{Y}_{jm}^{(\alpha)}(\hat{\mathbf{r}}')]^*, \quad (\text{A2})$$

where $\mathcal{T}(\hat{\mathbf{r}}, \hat{\mathbf{r}}')$ is the kernel of the T -matrix operator \mathcal{T} ; $T_j^{(m)} = T_j^{11}$ and $T_j^{(e)} = T_j^{22}$ are the Mie coefficients given by Eqs. (12) and (13), respectively. For non-absorbing particles, the energy absorption rate (34) vanishes and the T -matrix operator satisfies the unitarity relation:

$$2\mathcal{T}^\dagger \mathcal{T} + \mathcal{T}^\dagger + \mathcal{T} = 0. \quad (\text{A3})$$

The optical force then can be recast into the operator form:

$$\mathbf{F} = -\frac{\epsilon}{4\pi k^2} \langle ([\mathbf{E}_{\text{out}}^{(\text{inc})}]^* \cdot \mathcal{F} \mathbf{E}_{\text{out}}^{(\text{inc})}) \rangle_{\hat{\mathbf{r}}}, \quad (\text{A4})$$

$$\begin{aligned} \mathcal{F} &= 2\mathcal{T}^\dagger \hat{\mathbf{r}} \mathcal{T} + \hat{\mathbf{r}} \mathcal{T} + \mathcal{T}^\dagger \hat{\mathbf{r}} \\ &= [\hat{\mathbf{r}}, \mathcal{T}] + 2\mathcal{T}^\dagger \hat{\mathbf{r}} \mathcal{T} - 2\mathcal{T}^\dagger \mathcal{T} \hat{\mathbf{r}} = [\mathcal{T}^\dagger, \hat{\mathbf{r}}] + 2\mathcal{T}^\dagger \hat{\mathbf{r}} \mathcal{T} - 2\hat{\mathbf{r}} \mathcal{T}^\dagger \mathcal{T}, \end{aligned} \quad (\text{A5})$$

where we have used the unitarity relation (A3) to transform the expression for the operator \mathcal{F} and $[\mathcal{A}, \mathcal{B}] = \mathcal{A}\mathcal{B} - \mathcal{B}\mathcal{A}$ stands for the commutator of operators \mathcal{A} and \mathcal{B} . From Eq. (22),

it can readily be seen that multiplication of the far-field vector amplitude $\mathbf{E}_{\text{out}}^{(\text{inc})}(\hat{\mathbf{r}}, \mathbf{r}_p)$ by the unit vector $\hat{\mathbf{r}}$ can be replaced with the following differential (gradient) operation:

$$\hat{\mathbf{r}}\mathbf{E}_{\text{out}}^{(\text{inc})} = \tilde{\nabla}_p \mathbf{E}_{\text{out}}^{(\text{inc})}, \quad \tilde{\nabla}_p = -ik^{-1} \nabla_p = -ik^{-1} \left(\frac{\partial}{\partial x_p}, \frac{\partial}{\partial y_p}, \frac{\partial}{\partial z_p} \right). \quad (\text{A6})$$

Our next step is to derive the relations

$$- \langle ([\mathbf{E}_{\text{out}}^{(\text{inc})}]^* \cdot [\hat{\mathbf{r}}, \mathcal{T}]\mathbf{E}_{\text{out}}^{(\text{inc})}) \rangle_{\hat{\mathbf{r}}} = \tilde{\nabla}_p \langle ([\mathbf{E}_{\text{out}}^{(\text{inc})}]^* \cdot \mathcal{T}\mathbf{E}_{\text{out}}^{(\text{inc})}) \rangle_{\hat{\mathbf{r}}} = \tilde{\nabla}_p \langle ([\mathbf{E}_{\text{out}}^{(\text{inc})}]^* \cdot \mathbf{E}_{\text{out}}^{(\text{sca})}) \rangle_{\hat{\mathbf{r}}}, \quad (\text{A7})$$

$$\langle ([\mathbf{E}_{\text{out}}^{(\text{inc})}]^* \cdot \mathcal{T}^\dagger \mathcal{T} \hat{\mathbf{r}} \mathbf{E}_{\text{out}}^{(\text{inc})}) \rangle_{\hat{\mathbf{r}}} = \langle ([\mathbf{E}_{\text{out}}^{(\text{sca})}]^* \cdot \tilde{\nabla}_p \mathbf{E}_{\text{out}}^{(\text{sca})}) \rangle_{\hat{\mathbf{r}}} \quad (\text{A8})$$

that immediately follow from Eq. (A6) since the T -matrix operator and the Mie coefficients are both independent of the displacement vector \mathbf{r}_p .

Relations (A7)–(A8) and equation (A5) can now be substituted into formula (A4) to obtain the result in the final form:

$$\mathbf{F} = \frac{\epsilon}{4\pi k^2} \left\{ -2 \langle \hat{\mathbf{r}} ([\mathbf{E}_{\text{out}}^{(\text{sca})}]^* \cdot \mathbf{E}_{\text{out}}^{(\text{sca})}) \rangle_{\hat{\mathbf{r}}} + k^{-1} \text{Im} \left[\nabla_p \langle ([\mathbf{E}_{\text{out}}^{(\text{inc})}]^* \cdot \mathbf{E}_{\text{out}}^{(\text{sca})}) \rangle_{\hat{\mathbf{r}}} + 2 \langle ([\mathbf{E}_{\text{out}}^{(\text{sca})}]^* \cdot \nabla_p \mathbf{E}_{\text{out}}^{(\text{sca})}) \rangle_{\hat{\mathbf{r}}} \right] \right\}, \quad (\text{A9})$$

where the last two terms on the right hand side of Eq. (A9) represent a derivative dependent (gradient) contribution to the radiation force. It should be emphasized that the last term being generally non-conservative will contribute to the asymmetry of the stiffness matrix.